TÉCNICO LISBOA

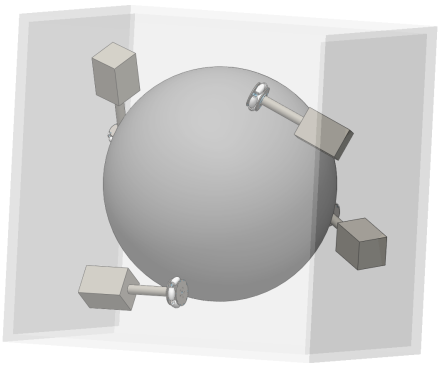

Reaction Sphere Actuator

António de Miranda Pombinho Amaral Craveiro

Thesis to obtain the Master of Science Degree in

Electrical and Computer Engineering

Supervisor: Prof. Dr. João Fernando Cardoso Silva Sequeira

Examination Committee

Chairperson: Prof. Dr. Horácio Cláudio de Campos Neto
Supervisor: Prof. Dr. João Fernando Cardoso Silva Sequeira
Member of the Committee: Prof. Dr. António Pedro Rodrigues de Aguiar

October 2015

Acknowledgments

I wish to express my sincere thanks to my supervisor, Prof. Dr. João Silva Sequeira, for his continuous support, unceasing patience and knowledge.

Furthermore I would also like to thanks my friends and family for their encouragement.

Personal Statement

This thesis has been a very interesting and educational journey to me. It allowed me to apply several concepts learned from my course and develop a critical thinking when designing a new device concept. Furthermore to translate and prove in mathematical terms the intuition that motivated the RSA study was extremely rewarding.

I hope this work can motivate further developments concerning RSAs.

Resumo

O controlo da orientação de satélites no espaço é um problema comum em engenharia aeroespacial. Para resolvê-lo consideram-se dispositivos de produção de binários de reacção. A esfera de reacção consiste numa nova aproximação a um dispositivo de produção de binários de reacção. Este dispositivo é composto por uma esfera, um sistema de actuação composto por quatro ou mais rodas holonómicas e uma estrutura envolvente. O contacto mecânico do sistema de actuação com a superfície esférica permite três graus de liberdade de rotação independentes à esfera assim como também garante o seu equilíbrio estático. Simultaneamente, o sistema de actuação está acoplado à estrutura envolvente. Ou seja, o sistema de actuação permite a criação de binários de reacção segundo qualquer eixo de rotação assim como assegura a transferência de momento angular a qualquer corpo acoplado ao dispositivo, e.g. satélites. Esta tese estuda a viabilidade e o desempenho da esfera de reacção. A controlabilidade da esfera de reacção é caracterizada a partir do seu modelo cinemático. Considera-se um exemplo de construção da esfera de reacção baseada num sistema de actuação com configuração tetraédrica regular, onde o respectivo Jacobiano descreve o movimento dos actuadores em relação ao movimento da esfera provando a não existência de singularidades. Por fim, analisa-se um modelo Simulink® do sistema de controlo da atitude de um satélite considerando dispositivos de produção de binários de reacção. Comparando o desempenho da esfera de reacção em função do trabalho mecânico a um sistema equivalente de rodas de inércia, concluem-se quais as suas vantagens.

Palavras-chave: Esfera de reacção, Rodas de inércia, Sistema de controlo de atitude de um satélite

Abstract

Satellite attitude control is a common problem in aerospace engineering. To solve it, reaction torque devices are usually considered. The reaction sphere actuator (RSA) is a novel device regarding reaction torque devices. The RSA is composed of a sphere, an actuation system and an outer shell. The mechanical rolling contact between the actuator system and RSA sphere surface, allows the sphere rotational motion and also achieves its static equilibrium. The actuator system composed of four or more holonomic wheels allows sphere three independent rotational DOF, allowing reaction torques generation according to any rotational axis. Moreover, the actuator system is coupled to an outer shell allowing angular momentum transfer to any RSA coupled body, e.g. satellites. This thesis performs a feasibility study proving the RSA construction eligibility as well as its performance analysis. The RSA controllability study is based upon its kinematic model considering rolling contact kinematics. Furthermore a RSA construction example is described considering an actuator system with a regular tetrahedral geometry configuration. The RSA Jacobian describes the RSA actuators motion for a desired reaction torque and proves its singularity-free property. Finally a performance analysis comparison between a RSA and an equivalent reaction wheel arrangement is depicted. Such analysis is performed according to a satellite attitude control scheme Simulink® model, measuring both RTDs mechanical work for the same desired control torques. The comparison of both simulation results shows the RSA concept benefits.

Keywords: Reaction torque device, Reaction sphere actuator, Satellite attitude control scheme

Contents

List of Tables

List of Figures

Nomenclature

Greek symbols

α	Angular acceleration.
Ω	Reference frame Angular Velocity.
ω	Body frame Angular Velocity.
τ	Torque.

Roman symbols

$\hat{\mathsf{w}}$	Rotational axis unit vector.
W	Distribution Matrix.
I_a	Motor armature current.
k	Holonomic wheel-Sphere radius ratio constant.
k_r	Motor transmission Gear ratio constant.
L_a	Motor armature inductance.
M	Force momentum.
q	Quaternion vector.
R_a	Motor armature resistance.
$S(\omega)$	Cross Product equivalent Matrix.
V_a	Motor armature voltage.
F	Force vector.
h	Angular momentum vector.
J	Inertia tensor matrix.
p	Linear momentum vector.

Subscripts

∞ Frobenius Norm.

s Sphere.

w Actuator wheel.

hub hub axis component.

i, j, k Computational indexes.

n Normal component.

$slip$ slip axis component.

x, y, z Cartesian components.

Superscripts

† Moore Penrose Pseudo-inverse.

$\hat{}$ Unit vector.

T Transpose.

Glossary

CMG	Control Moment Gyro
DOF	Degree of Freedom
ELSA	European Levitated Spherical Actuator
ESA	European Space Agency
PS	Power Supply
RSA	Reaction Sphere Actuator.
RTD	Reaction torque device
RW	Reaction wheel
SACS	Satellite Attitude Control System

Chapter 1

Introduction

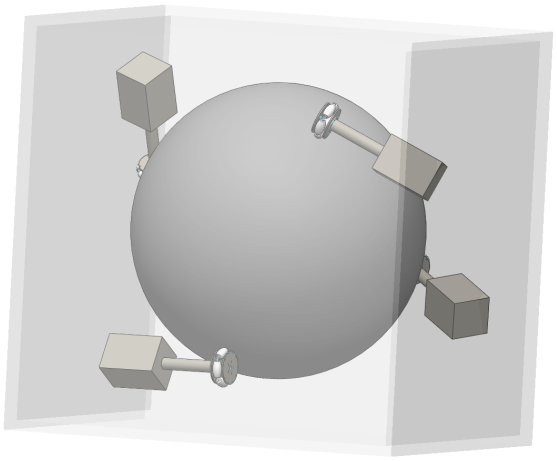

Figure 1.1: RSA with a regular tetrahedral geometry actuation system

This thesis analyses a reaction sphere actuator (RSA) device on its appliance to satellite attitude control problems. The referred device is a novel device taking advantage of spherical mass distribution for reaction torques production. A RSA kinematic and dynamic analysis verifies both the device physical feasibility and its benefits compared to other reaction torque devices (RTDs).

The RSA device, see Figure 1.1, is composed of a sphere, an actuation system and an outer shell (illustrated as a cubic case in Figure 1.1). The actuator system is composed of four or more holonomic wheels in mechanical contact with the sphere surface, conferring three independent rotational DOF to the sphere. Additionally, each holonomic wheel is actuated by a motor rigidly attached to the RSA outer shell, in fact, such coupling guarantees the sphere angular momentum transfer to any RSA coupled body, e.g. satellites. Furthermore, the actuator number and their contact points geometrical disposition determines the sphere static equilibrium, and its capability to rotate without displacing its geometric center with respect to an inertial frame described in the outer shell.

In Chapter 2 the RSA kinematic model is illustrated. The RSA kinematic analysis is divided in two steps. First, is studied a rolling sphere in a plane problem, studying the sphere controllability when non-coplanar angular speeds are used as sphere motion control inputs. In fact, differential geometry

concepts are used to describe the rolling mechanical contact between the sphere surface and holonomic actuators. Thereafter, a kinematic model for a holonomic mobile robot is considered due to its similarities compared to the actuator system geometry. The controllability of such model combined with the rolling sphere controllability enables the RSA controllability analysis.

Chapter 3 illustrates a satellite attitude dynamical model and control. First, a comparison of distinct satellite attitude formulations is considered, showing quaternion notation advantages for a SACS. Thereafter a satellite feedback attitude control is described allowing satellite reference attitude tracking. Moreover, a simple PD control law for satellite attitude control is presented, determining RTDs required control torques. Two types of RTDs are characterized, namely a RSA and a RW arrangement.

In Chapter 4 a set of distinct simulations are performed proving both satellite plant model validity and RTD performance. First, a simple SACS model without a RTD inclusion is simulated showing SACS attitude convergence for any attitude reference. Since this model doesn't account for RTDs limitations, any control torques given by the controller are feasible to apply to the satellite. Thereafter, a SACS with the inclusion of a RTD is analysed, allowing to compare both devices energy consumption in terms of mechanical work. Hence, ensuring RTDs equivalent physical parameters, a valid performance comparison can be considered.

Chapter 5 states this thesis main conclusions. Important aspects as the system physical feasibility and possible drawbacks are referred. The chapter ends with a list of topics that could be considered for future work.

1.1 Contributions

The demanding requirements in satellite attitude control problems are continuously being updated. As years go by, satellites become more complex with components being constantly optimized to fulfil space mission goals. Additionally, there's a major concern regarding components weight and energy consumption. Therefore, the RSA presents a novel concept considering such concerns.

The major contribution of such device, as it may be seen in Chapter 4, is to achieve similar reaction torque production compared to RW arrangements, with less system weight or equivalently, less energy consumption.

1.2 State-of-the-art

1.2.1 Reaction Wheels arrangements

Reaction torque devices are usually applied to control satellite attitude systems. The most common ones are reaction wheels, being essentially inertia disks rotating around a fixed axis. Such devices allow satellite attitude maneuvers due to angular momentum conservation. Furthermore, consider a rigid body in a torque-free situation with a RW coupled to its body. When RW angular velocity changes, its angular momentum also changes, causing a counter-movement performed by the overall rigid body,

see Appendix A. Hence, a single RW with its rotational axis fixed, may induce attitude changes to its coupled body around a single rotational axis vector. Consequently three-axis attitude motion capability can be achieved considering for instance a simple configuration composed of three RWs orthogonally disposed.

Besides reaction torque production capability, RWs also operate as momentum wheels, granting large amounts of stored angular momentum to satellites, thus reducing satellite external disturbances impact. Moreover, when external disturbances affect a satellite attitude, reaction wheels increase its angular momentum which eventually makes the RW to saturate. Therefore, occasionally there's a need to desaturate the satellite RWs, which can be performed with alternative RTDs, see [16].

RW arrangement dynamics can be analysed according Euler's equation, describing reaction torques for angular motion changes. See (1.1) for a RW arrangement dynamics general equation, note that (1.1) can still be expanded for three-dimensional rotations.

$$J \cdot \dot{\omega} + \omega \times (J \cdot \omega) = \tau \tag{1.1}$$

SACS software simulators with RW arrangements usually include RWs disturbances modelling, such as motor friction effects, motor bearings losses, RW body mass imbalances and others. For instance, [7] describes a RW model including electrical motors dynamic friction. Whereas [13] describes a mass imbalanced RW modelling and how it affects the SACS performance. Besides RW dynamical characteristics, SACS software simulators usually account for other satellite disturbances, such as solar radiation, gravity gradients, satellite flexibility, liquid slosh and others. An example of such kind of three-axis SACS software simulator is described in [21].

There are other approaches besides SACS software simulators, such as satellite physical model construction and performance measurement in a suitable testbed. The referred testbeds usually consist of a spherical air-bearing in which the satellite model stands, allowing it to have a limited angular motion range, which approximates the space free-torque environment. Furthermore, [27] shows a study of a satellite model analysis concerning RWs in a similar testbed.

RW arrangements can control independently each RW motion. Furthermore a RW arrangement overall torque[1] corresponds to the sum of all RWs torques.

RW arrangements vary both in RW number and geometry configuration, there's a common tendency to make these systems redundant, which has advantages regarding RW failure tolerance. Additionally, redundant RW arrangements usually allow a greater reaction torque capability, at the expense of requiring more mass. Hence, distinct RW arrangement geometry configurations have distinct performances. For instance, see [18] and [12] for a comparison of RW arrangements configurations composed of three and four RWs.

RW arrangements composed of more than three RWs are redundant, i.e. there are several RW torque combinations which result in the same overall resultant torque. Therefore, optimal criteria are used to choose one solution among all RW torque combinations. See [23] for two optimal criteria usually

[1] Torque has an important physical addition property that states that its overall value is independent of the RW geometrical location on the satellite frame. Therefore, RWs can be displaced in any geometrical location in the satellite frame.

Figure 1.2: Reaction Wheel regular tetrahedral configuration (obtained from ESA reports)

considered for RW arrangements.

A common four RWs configuration considers a regular tetrahedral geometry, see Figure 1.2.

RWs torque capability vary according to its inertial disk mass distribution and motor specifications. Such devices are usually applied for small satellites due to their mass/torque efficiency. Whereas heavier satellites and spacecrafts usually consider other RTDs. For instance, CMGs (control moment gyroscope) are often used for heavier satellites and spacecrafts. CMGs have more complex control techniques due to their gimbal lock possibilities, although providing higher power efficiency when compared to RW arrangements. A performance comparison study between RWs and CMGs is described in [31].

1.2.2 ELSA Project

ELSA project aims to build a magnetically levitated spherical actuator and is being researched by several European companies that work in the field of aerospace engineering. Despite ELSA project and RSA share the same goal (reaction torque production), there's a major difference concerning both actuators.

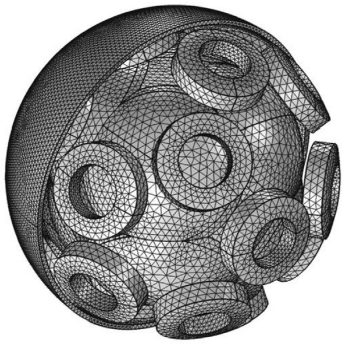

Figure 1.3: ELSA project spherical rotor (obtained from ELSA project website)

ELSA project actuator is composed of a magnetic spherical rotor that reacts to an induced electromagnetic field generated from an involving stator. Although being an innovative concept, it presents difficulties concerning the sphere rotor precise control, due to its complex magnetic dynamic model. The project has several goals that seeks to fulfil. The following list depicts ELSA project main goals, set in

accordance to ESA demands,

- torque capability larger than $0.4Nm$
- momentum storage in the order of $40Nms$
- high fidelity speed measurement
- reduced and guaranteed micro-vibration spectra

A magnetic spherical rotor presents some benefits compared to RSA rolling mechanical contact solution. For instance, it is absent of mechanical friction losses, mechanical vibrations and has a mass reduction due to the absence of physical actuators. Nevertheless, the production cost of a spherical magnetic rotor is probably higher compared to a RSA suitable sphere, due to its delicate building approach. Figure 1.3 illustrates an image of the spherical rotor concept depicting its magnetic cores.

1.2.3 Ballbots

Ballbots contributed to the motivation of this thesis due to their actuation system. Therefore, a brief description regarding a Ballbot model is considered.

Ballbots are essentially mobile robots consisting of inverted pendulums which stand on a sphere and move on a plane by actuating the sphere motion accordingly. An example of a Ballbot illustration is present in Figure 1.4, which corresponds to the *Rezero Ballbot*, see [9].

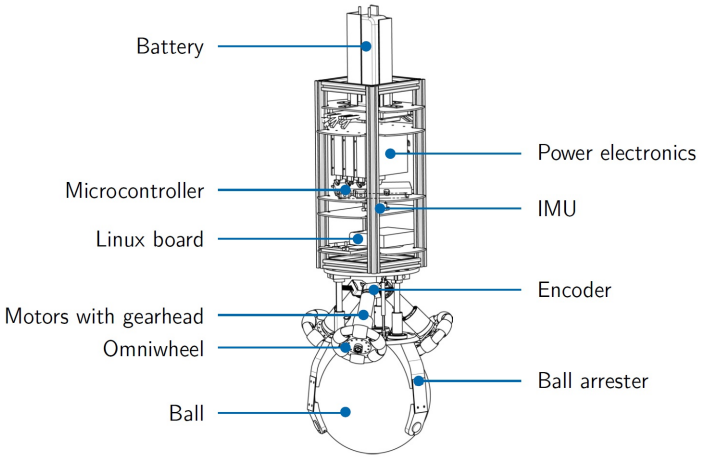

Figure 1.4: Rezero Ballbot (obtained from [9])

Several studies regarding Ballbot's dynamics were conducted by *Microdynamic Systems Laboratory at Carnegie Mellon University*. Both [9] and [17] show important considerations concerning Ballbot dynamical models which motivated the RSA concept development.

The RSA actuating system can actually be seen as an alternative application of the one used by Ballbots. Nevertheless, Ballbots aim to control an inverted pendulum by moving its sphere, whereas RSAs aim to move its internal sphere in order to produce reaction torques and apply them to RSA coupled bodies. Hence although their purposes are distinct there is a relation between both devices actuating systems since they both rely upon holonomic wheels.

Some of the following theoretical concepts and images have been taken in consideration according to [9].

The adopted Ballbot dynamical model relies upon Lagrangian dynamical formulation. Therefore, a full rigid bodies energy characterization composing the Ballbot is required. The use of a proper coordinate formulation for such kind of systems eases their model equations computation. Therefore, the system can be divided and analysed in three distinct independent planes easing its total dynamical model study.

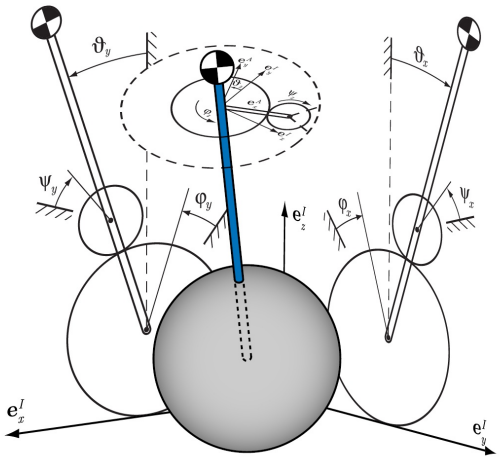

Figure 1.5: Ballbot Planar Model (obtained from [9])

Figure 1.5 illustrates the referred planes representing the system with respect to each DOF imposed by the holonomic actuators. This simplistic model assumes that each holonomic wheel corresponds to a virtual actuating wheel in each plane. This assumption eases model computations, although, it doesn't represent the actual reality of a holonomic wheel. Additionally, note that such planar description is also convenient given that a Ballbot uses only three holonomic wheels.

The planar system modelling approach has certain benefits regarding the three independent planar models. Two planes, namely the *xz*-plane and *yz*-plane, have several similarities. Whereas the third plane (*xy*-plane) describes the sphere rotation around the *z* axis.

The dynamic model formulation requires all rigid bodies identification composing the Ballbot system. Hence, in each independent plane there are three rigid bodies, the sphere, the actuating wheels (simplifying the omniwheel plus the respective motor) and the Ballbot body.

Thus, consider the following system describing parameters,

- $\vartheta_{x,y,z}$ - body orientation
- $\varphi_{x,y,z}$ - ball orientation
- $\psi_{x,y,z}$ - virtual actuating wheels angles

Using a minimal system of coordinates, the system pose can be fully described using three vectors as follows,

$$\vec{q}_{xy} = \begin{bmatrix} \varphi_z \\ \vartheta_z \end{bmatrix} \vec{q}_{yz} = \begin{bmatrix} \varphi_x \\ \vartheta_x \end{bmatrix} \vec{q}_{xz} = \begin{bmatrix} \varphi_y \\ \vartheta_y \end{bmatrix} \tag{1.2}$$

Hence the system energy equations can then be found according to Lagragian formulation using generalized coordinates, yielding,

$$\frac{d}{dt}\left(\frac{\partial T}{\partial \dot{\vec{q}}}\right)^T - \left(\frac{\partial T}{\partial \vec{q}}\right)^T + \left(\frac{\partial V}{\partial \vec{q}}\right)^T - \vec{f}_{NP} = 0 \tag{1.3}$$

where T, V and $\vec{f}_{NP}$ denote respectively the kinetic energy, potential energy and external forces. Where external forces refer to forces applied to the system, such as the motor torques induced in the holonomic actuators. Therefore, for each virtual plane describing the Ballbot there's an equation (1.3) describing the system energy equilibrium.

Additionally, each system plane equations can be written in matrix form, see (1.4).

$$M_x(\vec{q}, \dot{\vec{q}})\ddot{\vec{q}} + C_x(\vec{q}, \dot{\vec{q}}) + G_x(\vec{q}) = f_{NP} \tag{1.4}$$

where variables M_x, C_x, G_x and f_{NP} denote respectively the system mass and inertia matrix, the Coriolis forces matrix, the gravitational forces and the external forces. Given the system rigid bodies energy equations it's possible to obtain (1.4) matrices. Hence, solving (1.4) with respect to each plane minimal coordinates, describes how these variables change according to the system inputs, i.e. according to external forces.

1.2.4 Atlas Flight Simulator

The concept of inducing rotational motion to a sphere with holonomic wheels has also recently appeared for flight simulators. In fact, *Atlas Motion Platform* project developed by *Carleton University* is the first device of its kind. Similarly to the RSA device, a spherical body is rotated by holonomic wheels allowing three DOF rotation capability, without displacing its geometrical center. Nevertheless, there are certain differences comparing both devices. The atlas sphere static equilibrium is not ensured by the holonomic actuators, but due to a frame containing several bearings in contact with the sphere surface. Furthermore, the Altas device aims to create a flight simulator cockpit with full rotational capabilities that stands upon a parallel manipulator with three translation DOF. Such configuration creates a full six DOF capability realistic flight simulator.

Some Atlas kinematic model studies describe the system kinematic feasibility as well as possible actuator system geometries, see [20].

Although being a device which does not share the same goals as the RSA it allowed to motivate the RSA concept feasibility. Therefore, it represented an important analysis for the present thesis. Moreover, in kinematic terms the both systems *Jacobian*s are quite similar.

The state-of-the-art review shows us the nonexistence of a RTD with a spherical geometry with an actuation system based upon rolling mechanical contact with the sphere surface. Hence, the RSA presents itself as a novel device, relevant for analysis.

Chapter 2

Kinematic Model

This chapter is dedicated to the RSA kinematic analysis. Such analysis verifies the RSA internal sphere motion feasibility according to the actuating system geometry. Furthermore, the kinematic model equations allow the device controllability study, showing RSA eligibility in kinematic terms for satellite attitude control schemes. In other words the controllability proves the RSA capability to actuate the sphere according to any desired angular motion. Consequently, it can produce reaction torques with respect to any rotational vector. The kinematic model analysis is divided in two steps, namely, the motion analysis of a sphere rolling on a plane and a holonomic mobile robot.

Section 2.1 illustrates differential geometry concepts, describing rolling contact kinematics between the holonomic actuators and sphere surface. This concepts are relevant for computing the rolling sphere kinematic model. In fact, differential geometry concepts can describe any spheroid surface.

Section 2.2 applies differential geometry concepts for a spherical body. Hence, this Section describes the kinematic model of a sphere rolling on a plane, having as controlling inputs non-coplanar angular velocities vectors applied to its body. The model controllability can be proved showing the sphere ability to follow any trajectory on the plane surface with any orientation. Furthermore, such controllability is verified according to Lie Algebra concepts.

Section 2.3 illustrates an actuator system kinematic analysis. Due to their similarities with the actuator system, a holonomic mobile robot is considered. Hence, by inference, studying its kinematic model, some conclusions regarding the actuator system can be stated. The holonomic mobile robot full motion capability, i.e., its capability to follow any trajectory on the plane with any orientation proves the holonomic mobile robot controllability. Consequently, by analogy, the RSA actuator system controllability is also proven when it is moving on a plane surface.

Considering the kinematic analysis performed in Section 2.2 and 2.3 and following a logic reasoning the overall RSA kinematic model controllability is shown.

2.1 Rolling Contact Kinematics

Rolling contact kinematics is a relevant field of study in engineering, it allows to fully describe mechanical contact between two objects. These concepts have several practical applications, such as, characterizing robot hands grasp problems, mobile robots moving on regular surfaces and so on. Since this chapter concerns a RSA kinematic analysis, these theoretical concepts are useful for describing the RSA sphere angular motion capabilities. For a more detailed description see [26] and [5].

Consider an object in $\mathbb{R}^3$, where its surface is described according to a local coordinate map, as follows,

$$\boldsymbol{c} : U \subset \mathbb{R}^2 \rightarrow \mathbb{R}^3 \tag{2.1}$$

The map c illustrated in Figure 2.1 relates a point $(u, v) \in \mathbb{R}^2$ with a point $x \in \mathbb{R}^3$ belonging to the object surface, described with respect to reference frame O. Thus if only one map is required to parametrize the object surface, $\boldsymbol{c} : U \subset \mathbb{R}^2$ allows the entire object surface description. Some object surfaces parametrizations require the use of several maps, being the collection of such maps often called as atlas. Note that, the c mapping is sometimes referred as a parametrization, being both terms equivalent in differential geometry terms.

The following analysis concern regular surfaces parametrization, see [5] for a regular surface definition.

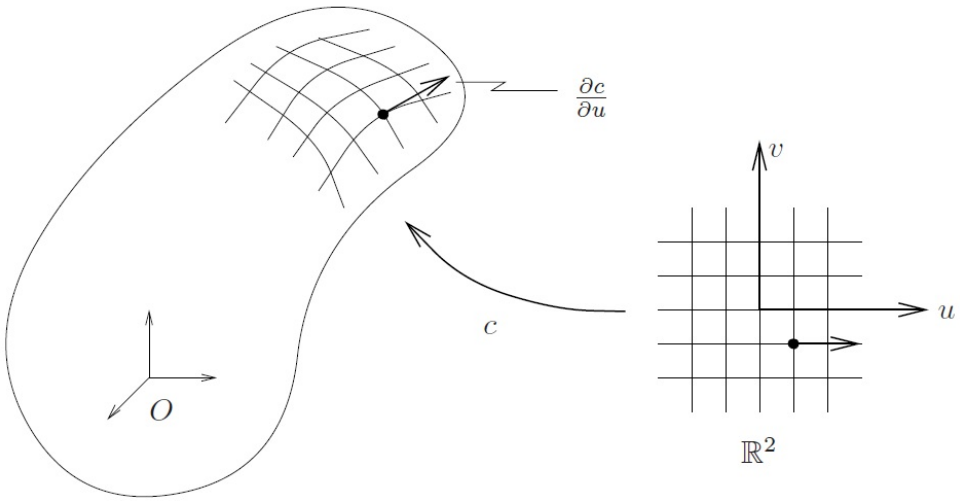

Figure 2.1: Object Surface (obtained from [26])

Any point belonging to a regular surface has a tangent plane defined by the set of vectors tangent to the object surface at the referred point. This tangent plane can be defined by two vectors $c_u := \frac{\partial c}{\partial u}$ and $c_v := \frac{\partial c}{\partial v}$. Hence, any point in surface $c(u, v)$ is described according to a linear combination of vectors c_u and c_v, evaluated at (u, v).

The surface area can be computed as the inner product of two tangent vectors lying on the referred surface. This product defines the parallelogram area with respect to those two vectors, thus it's feasible to compute the total area of an object surface. Such area computation is commonly related with a

surface *first fundamental form*, describing two tangent vectors inner product relation with the natural inner product on $\mathbb{R}^3$. Geometrically, the *first fundamental form* allows surface measurements such as curves lengths, tangent vectors angles, regions areas, and others. Therefore, using the *first fundamental form* all these computations can be performed without referring back to the ambient space $\mathbb{R}^3$ where the surface lies.

The *first fundamental form* can be computed in a local coordinate chart, being represented by a quadratic form $Ip : \mathbb{R}^2 \times \mathbb{R}^2 \to \mathbb{R}$ which takes two tangent vectors attached to a point $p = c(u, v)$ and gives their inner product, see (2.2).

$$I_p = \begin{bmatrix} c_u^T c_u & c_u^T c_v \\ c_v^T c_u & c_v^T c_v \end{bmatrix} \tag{2.2}$$

If the object surface map is orthogonal then matrix I_p is diagonal, furthermore a map orthogonality can be determined checking if c_u and c_v are *orthogonal*.

The *first fundamental form* can be used to define the surface metric tensor, given by the square root of the first fundamental form and it is usually applied to tangent vectors normalization. Matrix $M_p : \mathbb{R}^2 \to \mathbb{R}^2$ is then defined as positive definite and satisfies (2.3).

$$I_p = M_p.M_p \tag{2.3}$$

If I_p is orthogonal, then, matrix M_p is also diagonal, yielding,

$$M_p = \begin{bmatrix} \|c_u\| & 0 \\ 0 & \|c_v\| \end{bmatrix} \tag{2.4}$$

Surface S parametrization allows the definition of an outward pointing unit normal by taking the cross product between the vectors defining the tangent space. Thus, considering c_v and c_u vectors and identifying all normal unit vectors in $S \subset \mathbb{R}^3$, one obtains the map $N : S \to \mathbb{R}^3$ which essentially represents the unit sphere.

$$N(u, v) = \frac{c_u \times c_v}{\|c_u \times c_v\|} \tag{2.5}$$

Map $N : S \to S^2$ gives the unit normal at each point on S and is called *Gauss Map*. Where S^2 is defined as $S^2 = (x, y, z) \in \mathbb{R}^3$.

For smooth, orientable surfaces, the Gauss map is a well defined differential mapping, see [5] for a detailed Gauss map analysis. The *Gauss map* directional derivative defines a surface *second fundamental form*, measuring the surface curvature. Moreover in a local coordinate map it is represented as II_p, see (2.6).

$$II_p = \begin{bmatrix} c_u^T n_u & c_u^T n_v \\ c_v^T n_u & c_v^T n_v \end{bmatrix} \tag{2.6}$$

where $n = N(u, v)$ is the unit normal at a point on the surface and $n_u := \frac{\partial n}{\partial u}$, $n_v := \frac{\partial n}{\partial v}$.

It is convenient to scale the *second fundamental form* and define the curvature tensor for a surface.

For an orthogonal set of coordinates, the curvature tensor is a mapping $K : \mathbb{R}^2 \to \mathbb{R}^2$ defined as,

$$K_p = M_p^{-T} II_p M_p^{-1} = \begin{bmatrix} \frac{c_u^T n_u}{\|c_u\|^2} & \frac{c_u^T n_v}{\|c_u\|\|c_v\|} \\ \frac{c_v^T n_u}{\|c_u\|\|c_v\|} & \frac{c_v^T n_v}{\|c_v\|^2} \end{bmatrix} \tag{2.7}$$

Note that matrices M_p^{-1} and M_p^{-T} represent a scaling factor. Moreover, this curvature tensor can be thought of a measure of how the unit normal vector changes across the surface, projected on the tangent plane. If the surface is flat, then $n_u = n_v = 0$ and $K_p = 0$.

It's also possible to compute the curvature tensor in terms of a special coordinate frame called the normalized Gauss frame. This notation is suitable if the $c(u, v)$ parametrization is orthogonal, thus its respective Gauss frame can be simplified as follows,

$$\begin{bmatrix} x & y & z \end{bmatrix} = \begin{bmatrix} \frac{c_u}{\|c_u\|} & \frac{c_v}{\|c_v\|} & n \end{bmatrix} \tag{2.8}$$

And so, the curvature tensor can take advantage of this compact notation yielding,

$$K_p = \begin{bmatrix} x^T \\ y^T \end{bmatrix} \begin{bmatrix} \frac{c_u}{\|c_u\|} & \frac{c_v}{\|c_v\|} \end{bmatrix} \tag{2.9}$$

Now that the two first fundamental forms are defined, it only remains to define one last surface characterization metric which combined with the previous two, fully describes any regular surface.

The *torsion form* measures the curvature rate change along a surface S curve. Therefore, a surface *torsion form* is a measure of how the Gauss frame twists as one moves across the surface, again projected onto the tangent plane.

The *torsion form* computation only requires to know how either x or y change, since they are orthonormal. Therefore the *torsion form* is defined as,

$$T_p = y^T \begin{bmatrix} \frac{x_u}{\|c_u\|} & \frac{x_v}{\|c_v\|} \end{bmatrix} = \begin{bmatrix} \frac{c_v^T c_{uu}}{\|c_u\|^2\|c_v\|} & \frac{c_v^T c_{uv}}{\|c_u\|\|c_v\|^2} \end{bmatrix} \tag{2.10}$$

where x_u and x_v denote respectively the x and y partial derivatives with respect to u and v. Additionally $c_{uu} = \frac{\partial^2 c}{\partial u^2}$ and $c_{uv} = \frac{\partial^2 c}{\partial u \partial v}$ denote the mapping second order derivatives with respect to u and v.

Thus a solid regular surface can be described according to parametrizations (M_p, K_p, T_p), which are collectively referred as the surface geometric parameters.

Now that any regular surface can be parametrized, it is relevant to analyse the theoretical concepts describing two contact frames velocity in a rolling contact kinematic situation. Conveniently, the contact frame velocity can be computed according to its surface geometric parameters.

Let $p(t) \in S$ be a parametrization of a curve along an object surface coherent with its Gauss frame in every time instant.

Figure 2.2 shows the contact curve describing the contact point evolution with time. Assume that frame O is fixed with respect to the object. Therefore frame C motion must be characterized with respect to frame O, according to the rigid transformation $g_{oc} \in SE(3)$.

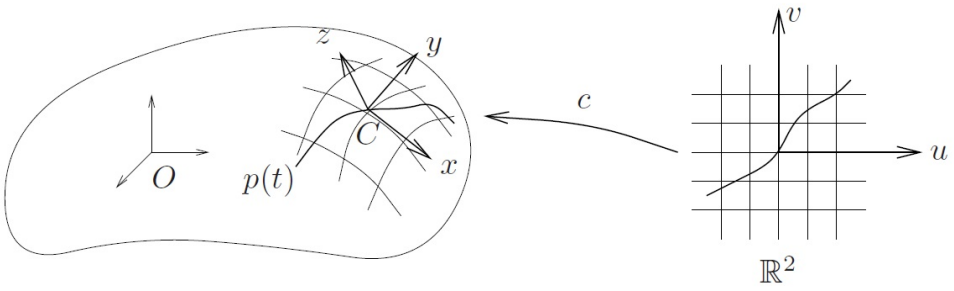

Figure 2.2: Contact curve (obtained from [26])

For simplicity, let physical contact between the object surfaces S_o and S_f, be always defined at a single point of contact. The kinematic model is based on the motion of this contact point relative to the objects motion. Hence, consider that $p(t)$ lies in a single coordinate map $U \to \mathbb{R}^3$, it is possible to represent the local coordinates as $\alpha(t) = c^{-1}(p(t))$. The position and orientation of the contact frame relative to the reference frame are given as,

$$\begin{aligned} p_{oc}(t) = p(t) = c(\alpha(t)) \\ R_{oc} = \begin{bmatrix} x(t) & y(t) & z(t) \end{bmatrix} = \begin{bmatrix} \frac{c_u}{\|c_u\|} & \frac{c_v}{\|c_v\|} & \frac{c_u \times c_v}{\|c_u\| \times \|c_v\|} \end{bmatrix} \end{aligned} \tag{2.11}$$

where R_{oc} corresponds to the rotation matrix from frame O to frame C. The linear body velocity is given by $v_{oc} = R_{oc}^T \dot{p_{oc}}$, see (2.12).

$$v_{oc} = \begin{bmatrix} x^T \\ y^T \\ z^T \end{bmatrix} \frac{\partial c}{\partial \alpha} \dot{\alpha} = \begin{bmatrix} x^T c_u & x^T c_v \\ y^T c_u & y^T c_v \\ z^T c_u & z^T c_v \end{bmatrix} \dot{\alpha} = \begin{bmatrix} M_p \dot{\alpha} \\ 0 \end{bmatrix} \tag{2.12}$$

As it can be seen from (2.12) there's no velocity along the z direction, since the object moves in a plane. The angular velocity equation is obtained according to (2.13).

$$\hat{\omega}_{oc} = R_{oc}^T \dot{R_{oc}} = \begin{bmatrix} x^T \\ y^T \\ z^T \end{bmatrix} \times \begin{bmatrix} \dot{x} & \dot{y} & \dot{z} \end{bmatrix} = \begin{bmatrix} 0 & x^T \dot{y} & x^T \dot{z} \\ y^T \dot{x} & 0 & y^T \dot{z} \\ z^T \dot{x} & z^T \dot{y} & 0 \end{bmatrix} \tag{2.13}$$

Additionally, $S(\omega)$ matrix allows to simplify (2.13), see (A.17) .

In terms of the surface geometric parameters (2.13) is defined as,

$$\hat{\omega}_{oc} = \left[\begin{array}{cc|c} 0 & -T_p M_p \dot{\alpha} & K_p M_p \dot{\alpha} \\ T_p M_p \dot{\alpha} & 0 & \\ \hline -(K_p M_p \dot{\alpha})^T & & 0 \end{array}\right] \tag{2.14}$$

Consider now Figure 2.3 illustrating two object surfaces in mechanical contact at a single point. With the background knowledge of contact frame velocity equations, the motion of each object frame can

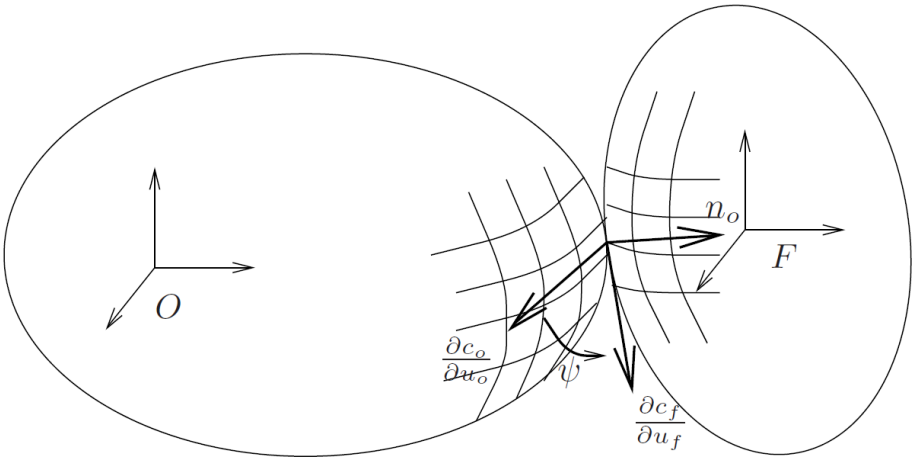

Figure 2.3: Two object contact (obtained from [26])

be characterized. This allows the contact point time evolution description with respect to the objects geometric parameters. For simplicity let the motion be contained in a single parametrization and the contact point be uniquely defined for both objects.

Let $p_o(t) \in S_o$ and $p_f(t) \in S_f$ be respectively the contact point position at time t with respect to frames O and F. Moreover, for each frame there is a map describing its surface, namely (c_o, U_o) and (c_f, U_f). Hence $\alpha_o = c_o^{-1}(p_o) \in U_o$ and $\alpha_f = c_f^{-1}(p_f)$ describe each object local coordinates. The ψ angle

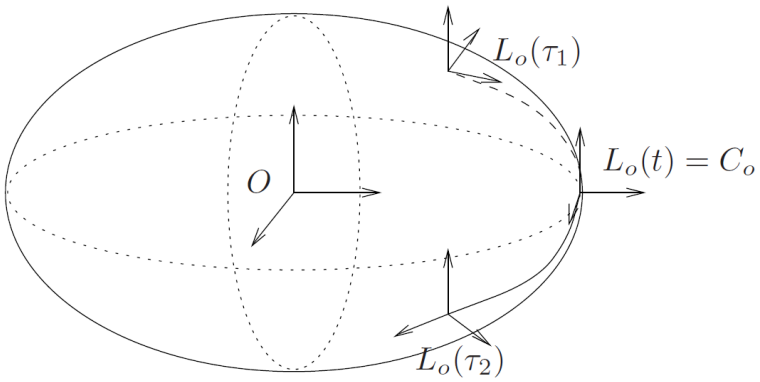

Figure 2.4: Local frames (obtained from [26])

denotes the rotation between the tangent vectors $\frac{\partial c_o}{\partial u_o}$ and $\frac{\partial c_f}{\partial u_f}$. Consequently the contact coordinate can be fully described by $(\alpha_o, \alpha_f, \psi)$. Frame O and F motion description at time t requires the definition of additional frames located at the contact point for each surface. Hence let $L_o(t)$ and $L_f(t)$ be the referred local coordinate frames, see Figure 2.4.

Finally, frame O and F contact motion equations yield,

$$\dot{\alpha_f} = M_f^{-1}(K_f + \tilde{K_o})^{-1}\left(\begin{bmatrix} -w_y \\ w_x \end{bmatrix} - \tilde{K_o}\begin{bmatrix} v_x \\ v_y \end{bmatrix}\right) \tag{2.15}$$

$$\dot{\alpha_o} = M_o^{-1} R_\psi (K_f + \tilde{K_o})^{-1} \left(\begin{bmatrix} -w_y \\ w_x \end{bmatrix} - K_f \begin{bmatrix} v_x \\ v_y \end{bmatrix} \right) \tag{2.16}$$

$$\dot{\psi} = w_z + T_f M_f \dot{\alpha_f} + T_o M_o \dot{\alpha_o} \tag{2.17}$$

$$v_z = 0 \tag{2.18}$$

$$\begin{aligned} \tilde{K_o} &= R_\psi K_o R_\psi \\ R_\psi &= \begin{bmatrix} cos(\psi) & -sin(\psi) \\ -sin(\psi) & -cos(\psi) \end{bmatrix} \end{aligned} \tag{2.19}$$

where ω_x,ω_y,ω_z,v_x,v_y and v_z are respectively the angular and linear velocities of object F with respect to object O. The previous motion equations proof can be found in [24].

Frenet-Serret formulas are also another form of describing the kinematic properties of a particle moving along a continuous, differentiable curve in three-dimensional Euclidean space $\mathbb{R}^3$. Hence this rolling kinematic model could also be computed according to such formulas, see [5].

Having stated all theoretical concepts required to devise the motion equations regarding a rolling contact between two objects, lets consider their application to the RSA sphere case.

As referred before, due to the surface complexity of a holonomic actuator the RSA kinematic model analysis is divided into two steps, namely the motion of a rolling sphere on a plane and a holonomic mobile robot. The rolling sphere on a plane doesn't match exactly the RSA kinematic behaviour, nevertheless in combination with the kinematic analysis of the actuator system, it is possible to infer the RSA controllability.

Consider a r radius sphere, having its surface parametrized according to a single spherical coordinates map. A frame located on the sphere surface can be described by a rotation matrix with respect to u and v angles.

Figure 2.5 shows a parametrization defined as, $U = (u, v) : -\frac{\pi}{2} < u < \frac{\pi}{2}, -\pi < v < \pi$, where the contact point coordinates in the sphere frame Σ_o are obtained according to the following vector,

$$c(u_o, v_o) = \begin{bmatrix} -rsin(u_o)cos(v_o) \\ rsin(v_o) \\ -rcos(u_o)cos(v_o) \end{bmatrix} = R_y(u_o) R_x(v_o) \begin{bmatrix} 0 \\ 0 \\ -r \end{bmatrix} \tag{2.20}$$

Vector (2.20) defines any position on the sphere surface with respect to angles u_o and v_o. Hence, the sphere surface tangent vectors can be computed considering the partial derivatives of c with respect to u_o and v_o, yielding,

$$c_u = \frac{\partial c}{\partial u_o} = \begin{bmatrix} -rcos(u_o)cos(v_o) \\ 0 \\ rsin(u_o)cos(v_o) \end{bmatrix}, c_v = \frac{\partial c}{\partial v_o} \begin{bmatrix} rsin(u_o)sin(v_o) \\ rcos(v_o) \\ rcos(u_o)cos(v_o) \end{bmatrix} \tag{2.21}$$

It can be easily verified that $c_u^T c_v = 0$, proving the map orthogonality. The sphere surface metric,

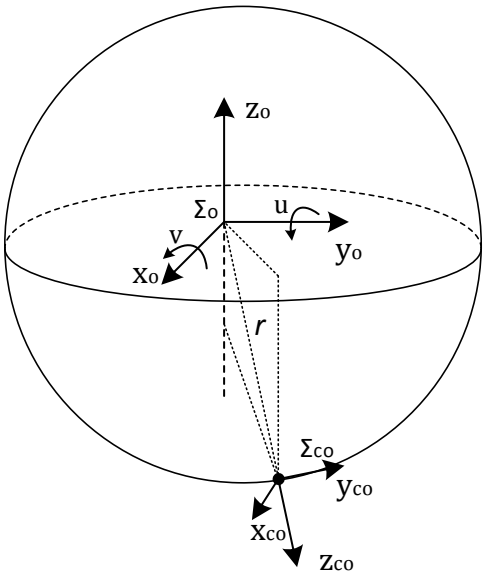

Figure 2.5: Sphere parametrization

curvature and torsion tensors are respectively given by:

$$M_o = \begin{bmatrix} rcos(v_o) & 0 \\ 0 & 1 \end{bmatrix}, K_o = \begin{bmatrix} \frac{1}{r} & 0 \\ 0 & \frac{1}{r} \end{bmatrix}, T_o = \begin{bmatrix} \frac{-tan(u_o)}{r} & 0 \end{bmatrix} \tag{2.22}$$

Having described the sphere geometric parameters it is still required to find the geometric parameters of plane frame O. Since a plane is a flat surface, its geometric parameters are quite trivial to compute. The map coordinates are defined as u_a and v_a, thus the plane surface local coordinates are chosen to be $c(u_a, v_a) = (u_a, v_a, 0)$. Therefore, the plane metric, curvature and torsion tensors are described by (2.23).

$$M_a = \begin{bmatrix} 1 & 0 \\ 0 & 1 \end{bmatrix}, K_a = \begin{bmatrix} 0 & 0 \\ 0 & 0 \end{bmatrix}, T_a = \begin{bmatrix} 0 & 0 \end{bmatrix} \tag{2.23}$$

Figure 2.6 shows the coordinate frames required for motion problem formulation. Let Σ_b be the world frame, Σ_o a fixed frame at the sphere geometric centre and Σ_a a fixed frame fixed at the contact plane. Additionally, at contact point, there are two contact frames, namely Σ_{co} for the sphere and Σ_{ca} for the plane. Figure 2.6 illustrates all frames used for obtaining the kinematic model.

Since $c(u_o, v_o)$ defines the Gaussian frame Σ_{co} whose orientation with respect to Σ_o is

$$R^o_{co} = \begin{bmatrix} \frac{c_u}{\|c_u\|} & \frac{c_v}{\|c_v\|} & \frac{c_u \times c_v}{\|c_u \times c_v\|} \end{bmatrix} \tag{2.24}$$

Knowing the values of c_u and c_v it's possible to rewrite the matrix with respect to these vectors, as

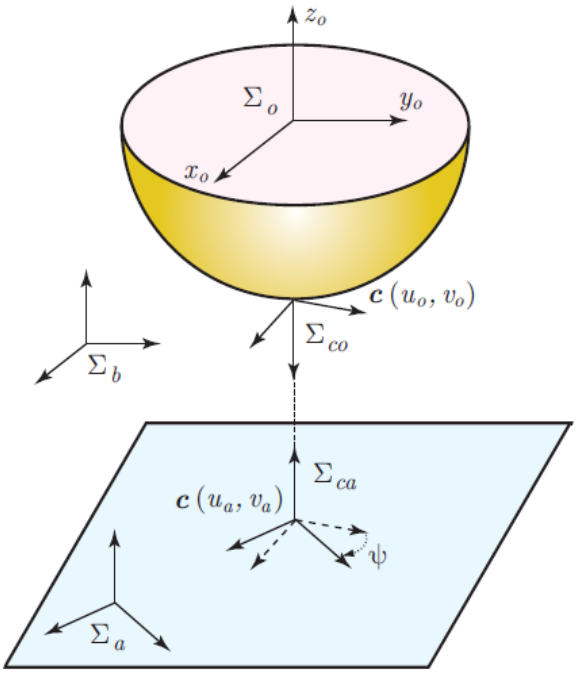

Figure 2.6: Sphere frames (obtained from [29])

follows

$$R^o_{co}(u_o, v_o) = \begin{bmatrix} -cos(u_o) & sin(u_o)sin(v_o) & -sin(u_o)cos(v_o) \\ 0 & cos(v_o) & sin(v_o) \\ sin(u_o) & cos(u_o)sin(v_o) & -cos(u_o)cos(v_o) \end{bmatrix} \tag{2.25}$$

Matrix (2.25) can alternatively be seen as the composition of three rotation matrices, as follows,

$$R^o_{co}(u_o, v_o) = R_y(u_o)R_x(v_o)R_y(\pi) \tag{2.26}$$

Let's define R^b_o, i.e. the sphere frame orientation matrix relative to the world frame. First, consider the rotation from Σ_{co} to Σ_{ca} which results in the superimposition of its axes. The combination of two specific rotation matrices achieves the referred frames axes superimposition, namely $R_y(\pi)$ and $R_z(\psi)$. Thus, the orientation of Σ_{co} relative to Σ_{ca} is defined as

$$R^b_{co}R_y(\pi)R_z(\psi) = R^b_{ca} \tag{2.27}$$

where,

$$\begin{aligned} R_y(\pi)R_z(\psi) &= \begin{bmatrix} -cos(\psi) & sin(\psi) & 0 \\ sin(\psi) & cos(\psi) & 0 \\ 0 & 0 & -1 \end{bmatrix} \\ R_y(\pi) &= \begin{bmatrix} -1 & 0 & 0 \\ 0 & 1 & 0 \\ 0 & 0 & -1 \end{bmatrix} \end{aligned} \tag{2.28}$$

The ψ angle is defined between Σ_{co} and Σ_{ca} x-axes and has its angle rotation opposite to the right hand

rule.

Let us assume that frame Σ_a coincides with Σ_b and that frame Σ_{ca} is coherent with Σ_a. From closing the kinematic chain associated with the coordinate frames one obtains,

$$R_o^b R_{co}^o R_y(\pi) R_z(\psi) = R_{ca}^b \equiv I \tag{2.29}$$

Hence

$$R_o^b R_y(u_o) R_x(v_o) R_z(\psi) = I \tag{2.30}$$

The sphere orientation matrix is then given by,

$$R \equiv R_o^b = R_z^T(\psi) R_x(v_o)^T R_y(u_o)^T \tag{2.31}$$

Let $\tilde{v} = \begin{bmatrix} \tilde{v_x} & \tilde{v_y} & \tilde{v_z} \end{bmatrix}$ and $\tilde{w} = \begin{bmatrix} \tilde{w_x} & \tilde{w_y} & \tilde{w_z} \end{bmatrix}$ be respectively, the translational and angular velocity of Σ_{co} relative to Σ_{ca}. The physical interpretation of Σ_{co} angular velocities can be projected into Σ_b. Hence the angular velocity vector, $w_o = \begin{bmatrix} w_x & w_y & w_z \end{bmatrix}$ is obtained from the rotation between these two frames as follows,

$$\tilde{w} = R_y(\pi) R_z(\psi) w_o \tag{2.32}$$

Substituting (2.20), (2.22) and (2.22) in (2.15), (2.16), (2.17) and (2.19) the kinematic model motion equations yield,

$$\begin{bmatrix} \dot{u_a} \\ \dot{v_a} \\ \dot{u_o} \\ \dot{v_o} \\ \dot{\psi} \end{bmatrix} = \begin{bmatrix} 0 & -r & 0 \\ -r & 0 & 0 \\ \frac{-sin(\psi)}{cos(v_o)} & \frac{-cos(\psi)}{cos(v_o)} & 0 \\ -cos(\psi) & sin(\psi) & 0 \\ -sin(\psi)tan(v_o) & -cos(\psi)tan(v_o) & -1 \end{bmatrix} \begin{bmatrix} w_x \\ w_y \\ w_z \end{bmatrix} \tag{2.33}$$

Note that (2.33) uses the contact frame angular velocity projections defined in (2.32).

This Section shows the importance of rolling contact kinematics for analysing the kinematic model of any two objects with regular surfaces. Hence, besides the sphere rolling on a plane other spheroids can be considered.

2.2 Controllability of the Sphere Kinematic model

The rolling sphere controllability can be studied according to its kinematic model, see [28] for a controllability definition. Moreover, this section analyses the controllability according to some Lie Algebra concepts, see [26] and [30] for further details.

The kinematic model (2.33) is a 3-inputs 5-outputs system, thus it contains three vector fields describing three independent motions.

Alternatively the kinematic model (2.33) can be seen with respect to its vector fields, as follows,

$$\dot{q} = g_1(q)u_1 + g_2(q)u_2 + g_3(q)u_3 \tag{2.34}$$

where

$$g_1(q) = \begin{bmatrix} -r \\ 0 \\ \frac{-sin(\psi)m}{cos(v_o)} \\ -cos(\psi) \\ -sin(\psi)tan(v_o) \end{bmatrix}, g_2(q) = \begin{bmatrix} 0 \\ -r \\ \frac{cos(\psi)m}{cos(v_o)} \\ sin(\psi) \\ -cos(\psi)tan(v_o) \end{bmatrix}, g_3(q) = \begin{bmatrix} 0 \\ 0 \\ 0 \\ 0 \\ -1 \end{bmatrix} \tag{2.35}$$

Using only three vector fields it is not possible to control the 5-output variables independently. To make this achievable five vector fields are required. The controllability Lie algebra matrix (composed by the model n vector field vectors) enables the model controllability study according to *Chow* Theorem. This theorem states that if the controllability Lie algebra matrix (dimension $m \times n$) is full rank, one can control the m model outputs independently. For a *Chow* theorem proof see [26]. Using Lie bracket operators it's possible to compute two more vector fields from combinations of the existing ones.

The Lie bracket of two vector fields f and g is defined as,

$$[f, g](q) = \frac{\partial g}{\partial q} f(q) - \frac{\partial f}{\partial q} g(q) \tag{2.36}$$

Lie algebra computations were performed with MATLAB® symbolic language easing Lie Algebra bracket combinations calculations. Therefore, considering Lie bracket operators for the existing vector fields in (2.33) it is possible to compute two new ones. Hence, if such vector fields combined with the ones in (2.33) result in a full rank controllability Lie algebra matrix, then the model controllability is proven. For simplicity let the sphere radius be unitary.

One example of a valid *controllability Lie algebra* matrix is defined as,

$$\begin{bmatrix} [g_1] & [g_2] & [g_3] & [g_1, g_2] & [g_1, [g_1, g_2]] \end{bmatrix} \tag{2.37}$$

Which in its explicit form is given by,

$$\begin{bmatrix} 0 & -1 & 0 & 0 & 0 \\ -1 & 0 & 0 & 0 & 0 \\ \frac{-sin(\psi)}{cos(v_o)} & \frac{cos(\psi)}{cos(v_o)} & 0 & \frac{-(2sin(v_o)(2sin^2(\psi)-1))}{(sin^2(v_o)-1)} & \frac{cos(\psi)(16cos^2(\psi)-12)-cos^2(v_o)cos(\psi)(12cos^2(\psi)-11)}{cos^3(v_o)} \\ -cos(\psi) & sin(\psi) & 0 & 0 & -sin(\psi) \\ -sin(\psi)tan(v_o) & -cos(\psi)tan(v_o) & -1 & 1 & cos(\psi)tan(v_o) \end{bmatrix} \tag{2.38}$$

Computing (2.38) rank, one gets that it is equal to five, which as stated before proves that a sphere actuated by three angular velocity inputs is controllable. It is also interesting to study the controllability for the same system considering only two angular velocities inputs, for instance, w_x, w_y. Computing matrix (2.39) rank, one finds that the system is also controllable.

$$\begin{bmatrix} [g_1] & [g_2] & [g_1, g_2] & [g_1, [g_1, g_2]] & [g_2, [g_2, g_1]] \end{bmatrix} \tag{2.39}$$

Nevertheless, a sphere motion controlled with only two angular velocities may show complex maneuvering regarding its angular trajectory, which may be undesirable for the actuator system.

The sphere rolling on a plane controllability analysis presents a valid feasibility proof of the RSA kinematic goals. Hence controlling the model three inputs $(\omega_x, \omega_y, \omega_z)$ any trajectory and orientation of the sphere rolling on a plane can be achieved.

2.3 Controllability of the Actuator System

This section illustrates the RSA actuator system analysis regarding its kinematic model and controllability. The actuator system controllability is determined according to the kinematic model analysis of an equivalent holonomic mobile robot.

There are several types of holonomic actuators that could be considered for the RSA device. In fact, this section describes a kinematic model for a mobile robot composed of holonomic wheels without strictly specifying its roller axis angle or its wheel geometrical arrangement. Hence such model allows a general kinematic analysis compatible with distinct RSA actuating systems.

Mobile robots generally differ in wheel type and geometrical wheel disposition. In fact, each distinct mobile robot configuration yields different kinematic models, moreover [3] analyses mobile robot distinct configurations and respective kinematic models.

Figure 2.7 shows a three-wheeled holonomic mobile robot with its wheel frames depicted. Let us assume that each wheel rotational axis is fixed with respect to each other, and lie always parallel to the fixed ground plane P described by k normal unit vector. Moreover each hth holonomic wheel is indexed from 1 to N.

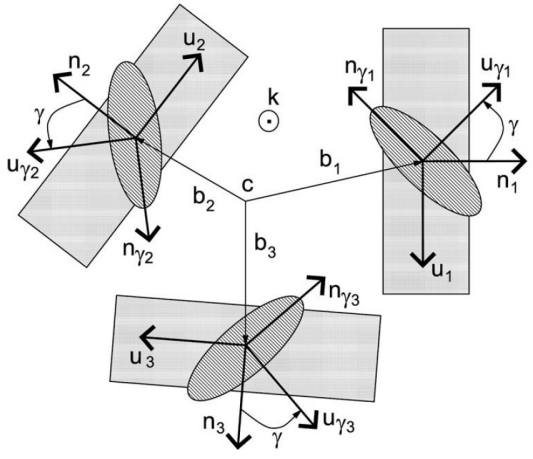

Figure 2.7: Three-wheel omnidrive robot (obtained from [11])

The ellipses represented in Figure 2.7 describe the wheel roller in contact with the ground plane P. Furthermore the wheel roller axes unit vectors are defined as $n_{\gamma h} : \|n_{\gamma h}\| = 1$ and $u_{\gamma h} : \|u_{\gamma h}\| = 1$. In fact, $n_{\gamma h}$ denotes the wheel roller axis and $u_{\gamma h} := n_{\gamma h} \times k$ the wheel roller instantaneous tangent velocity direction. Additionally the wheel hub axis unit vector (wheel main rotation axis) is denoted as

$n_h : \|n_h\| = 1$. Whereas $u_h : n_h \times k$ denotes the wheel instant tangent velocity direction. Moreover Figure 2.7 also illustrates each wheel position in the body fixed frame characterized by b_h. Additionally assume that all wheels have the same shape and radius ρ.

The holonomic mobile robot motion analysis considers the reference frame to be located at c (see Figure 2.7), describing the robot movement. Hence let's compute the mobile robot angular and linear velocities of such reference frame with respect to an inertial frame. Consider v_c to be the robot center linear velocity and ω_k to be its angular velocity. Whereas vector v_h denotes the linear velocity at each holonomic wheel frame. These v_h velocities are given by:

$$v_h = v_c + \omega_k \times b_h \tag{2.40}$$

See Appendix A for further details regarding (2.40).

For a perfect rolling situation, the velocity $v = v_h$ will be physically performed by the roller rotation around $n_{\gamma h}$ plus the wheel rotation around n_h. Considering that $n_{\gamma h}$ and n_h are not aligned, i.e. $\gamma \neq (2\upsilon + 1) \cdot 90 \ \deg$, where υ is an integer. The resultant velocity is given by,

$$v_h = \alpha u_{\gamma h} + \beta u_h \tag{2.41}$$

implying

$$n_h^T v_h = \alpha (n_h^T u_\gamma) \tag{2.42}$$

$$n_{\gamma h}^T v_h = \beta (n_{\gamma h}^T u_h) \tag{2.43}$$

where α and β are integers. Consequently combining these three equations yields,

$$v_h = \frac{n_h^T v_h}{n_h^T u_{\gamma h}} u_{\gamma h} + \frac{n_{\gamma h}^T v_h}{n_{\gamma h}^T u_h} u_h \tag{2.44}$$

Note that for mobile robot inducing motion purposes, the first velocity term on the right hand side of (2.44) depending on the roller rotation around $n_{\gamma h}$ is completely passive. Therefore, only the second term regarding the wheel rotation around n_h is assumed to be actively produced by a motor. Assuming a perfect rolling situation, the mapping between the joint speed $\dot{q}$ and the corresponding hub velocity of any wheel yields,

$$\frac{n_{\gamma h}^T v_h}{n_{\gamma h}^T u_h} = \rho \dot{q} \tag{2.45}$$

where it is has been explicitly assumed that the contribution of v_h in the direction of u_h described in (2.46) does not contribute to $\rho \dot{q}$.

$$\frac{n_h^T v_h}{n^T u_{\gamma h}} u_{\gamma h}^T u_h \tag{2.46}$$

Substituting (2.40) into (2.45), and having in mind that $n_{\gamma h}^T u_h = -cos\gamma$ for any h wheel, it follows that,

$$-\frac{1}{cos\gamma} n_{\gamma h}^T v_c + \frac{1}{cos\gamma} n_{\gamma h}^T \ S(b_h) \ \vec{k}\omega = \rho \dot{q}_h \tag{2.47}$$

see (A.17) for further details regarding $S(b_h)$. Considering the vectors projection on a common body-fixed frame with its third axis equal to $k \neq P$, the term $n_{\gamma h}^T S(b_h)\vec{k}$ results in

$$n_{\gamma h}^T S(b_h)\vec{k} = n_{\gamma x h} b_{y h} - n_{\gamma y h} b_{x h} = -b_h^T u_{\gamma h} \tag{2.48}$$

A simplified model of (2.47) in a general matrix form, can be seen as,

$$M \begin{bmatrix} v_c \\ \omega \end{bmatrix} = \rho \dot{q} cos\gamma \tag{2.49}$$

where

$$M = - \begin{bmatrix} n_{\gamma x 1} & n_{\gamma y 1} & b_1^T u_{\gamma 1} \\ n_{\gamma x 2} & n_{\gamma y 2} & b_2^T u_{\gamma 2} \\ \vdots & \vdots & \vdots \\ n_{\gamma x N} & n_{\gamma y N} & b_N^T u_{\gamma N} \end{bmatrix} \in \mathbb{R}^{N \times 3} \tag{2.50}$$

where vector $\dot{q} \in \mathbb{R}^{N \times 1}$ denotes the joint velocities vector. Equations (2.49) and (2.50) represent the general kinematics model of a holonomic wheeled vehicle with N wheels. The kinematic model controllability is related with the M matrix shape. Hence to prove that the system is in fact controllable two conditions must be satisfied,

1. $cos\gamma \neq 0$
2. rank $M = 3$

Furthermore, the mobile robot desired motion can be computed as,

$$\dot{q_d} = \frac{1}{\rho cos\gamma} M \begin{bmatrix} v_c \\ \omega_d \end{bmatrix} \tag{2.51}$$

The general holonomic mobile robot kinematic model and its controllability analysis verifies an equivalent actuator system controllability. Note that, besides the actuator wheels angle γ, the wheel position is also relevant to the kinematic model.

Furthermore a simple equilateral triangle wheel arrangement is proven to be controllable, see [3]. Hence such geometry is suitable for an RSA actuation system. Figure 2.8 illustrates the referred geometry.

The kinematic models of both problems and their respective controllability enable us to establish a connection between their results. Moreover the RSA controllability relies upon a logic reasoning considering both problems.

Subsection 2.2 shows the rolling sphere controllability when three non-coplanar angular velocity vectors control the sphere motion. Additionally, such angular velocities are obtained according to an actuator system composed of holonomic wheels. Furthermore Subsection 2.3 defines a general kinematic model framework and controllability analysis for distinct actuator systems, being an equilateral triangle configuration a valid geometry. Hence since the actuator system wheels are in contact with the sphere

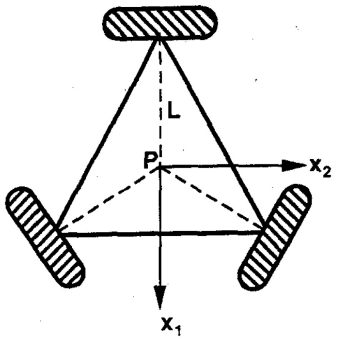

Figure 2.8: Three-Swedish-wheel triangular mobile robot (obtained from [3])

surface which is parametrized by a single $\mathbb{R}^2$ regular map, by inference the actuation system can also be controllable for a sphere surface. If it eases the understanding of this logic reasoning, consider an infinitely large sphere and an actuator system in mechanical contact with its surface. Therefore since the actuation system dimension is small compared to the sphere dimension, from an actuator point of view the sphere surface appears to it as a plane surface, thus being controllable. For an actuator system and sphere similar dimensions the actuators configuration must adapt the sphere surface being no longer in a plane configuration, although being still controllable.

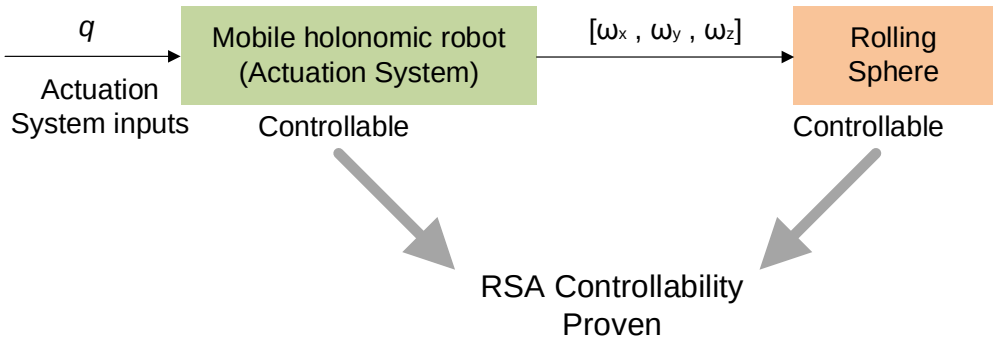

Figure 2.9: RSA Controllability

Considering the previous reasoning, the RSA system controllability is proven, see Figure 2.9, i.e. the RSA internal sphere is able to follow any angular motion and consequently produce reaction torques in every direction.

Chapter 3

Satellite Attitude Dynamical Model and Control

Satellite attitude dynamic models analyses its motion behaviour with respect to control torques applied to its frame. Control torques are usually produced by reaction torque devices (RTDs), which for this analysis are considered to be a RSA device or a RW arrangement.

Section 3.1 describes a satellite dynamical model computation without the RTD characterization. Moreover such model requires a satellite attitude formulation. Hence three different attitude formulations are analysed, stating their advantages and disadvantages. Quaternion notation is considered to be suitable for satellite attitude description due to its computational benefits. Thereafter a SACS dynamical model according to Euler's equations is described. Consequently a feedback closed-loop scheme with a simple *PD* control law ensures the satellite target attitude tracking. Simulink® software can be used for simulating the referred model, see Chapter 4.

Section 3.2 characterizes RTDs used in satellite attitude control, namely a RSA and a RW arrangement. The RSA actuator system geometry choice determines the RSA *Jacobian*. Therefore, due to its geometrical balance benefits, an actuator system according to a regular tetrahedral geometry is considered. The correspondent *Jacobian* for the referred geometry gives the actuators unique motion combination for a desired sphere angular motion as well as prove the RSA singularity-free property. Additionally, a brief explanation concerning a DC motor model suitable for being applied to a RSA model is described. Consequently, the motor "load sharing" problem is also covered presenting an important RSA feature. Analogously to the RSA device, a similar approach for a RW arrangement is devised. Nevertheless, oppositely to the RSA each RW angular motion is independent with respect to all others. For redundant n RW arrangement (i.e. $n > 3$) there are several valid RWs motion combinations that fulfil a given output torque. Therefore optimal criteria are required to choose one solution among all RW torque combinations. Two distinct torque optimal criteria are usually used for redundant RW arrangements, they are based upon the L_2 and L_∞ norms.

3.1 Satellite Modelling

3.1.1 Satellite attitude

Satellite attitude control schemes allow satellites to reach target attitudes according to control torques. Consequently is required to chose a satellite attitude formulation for SACSs.

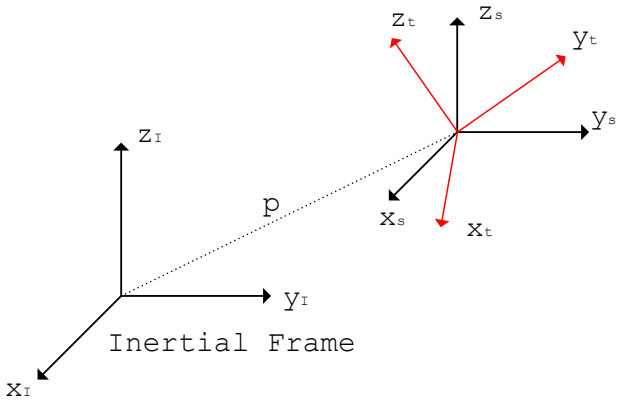

Figure 3.1: Satellite attitude reference frames

Figure 3.1 illustrates three frames describing the satellite attitude error problem. Frame $[x_I, y_I, z_I]$ refers to an inertial frame, whereas $[x_s, y_s, z_s]$ and $[x_t, y_t, z_t]$ are respectively the satellite current frame and satellite target frame both with respect to inertial frame I. For simplicity the translational vector p is assumed to be zero which means that the satellite geometrical center is coherent with the inertial frame origin.

Rotation matrices $[A_s]$ and $[A_t]$ describe respectively the satellite current and target frames rotations with respect to the inertial frame. Consider an arbitrary vector $a = [a_x\ a_y\ a_z]$ defined in the inertial frame. Using matrices $[A_s]$ and $[A_t]$ the referred vector can be described both in satellite and target frame as follows,

$$\begin{aligned} a_s &= [A_s]a \\ a_t &= [A_t]a \end{aligned} \tag{3.1}$$

Combining both equations in (3.1) yields,

$$a_s = [A_s][A_t]^{-1}a_t = [A_s][A_t]^T a_t = [A_e]a_t \tag{3.2}$$

If both vectors a_t and a_s are equivalent in satellite and target frame, then $[A_e]$ becomes identity since both frames coincide with each other. Matrix $[A_e]$ is referred as the *error attitude matrix*, describing the error between satellite current orientation and target orientation.

For further clarification, consider matrix $[A_e]$ full expression described in (3.3).

$$[A_e] = \underbrace{\begin{bmatrix} a_{11s} & a_{12s} & a_{13s} \\ a_{21s} & a_{22s} & a_{23s} \\ a_{31s} & a_{32s} & a_{33s} \end{bmatrix}}_{[A_s]} \underbrace{\begin{bmatrix} a_{11t} & a_{21t} & a_{31t} \\ a_{12t} & a_{22t} & a_{32t} \\ a_{13t} & a_{23t} & a_{33t} \end{bmatrix}}_{[A_t]^T} = \begin{bmatrix} a_{11e} & a_{12e} & a_{13e} \\ a_{21e} & a_{22e} & a_{23e} \\ a_{31e} & a_{32e} & a_{33e} \end{bmatrix} \tag{3.3}$$

Consequently satellite current and target frames coincide when $[A_e]$ off-diagonal elements become zero and the diagonal elements become unity. Therefore, ensuring that $a_{12e} = 0$, $a_{13e} = 0$ and $a_{23e} = 0$, makes both the target and current satellite frames equivalent.

There are at least three distinct attitude descriptions for a given body frame with respect to an inertial frame,

- Euler angles rotation matrix
- *Euler axis* of rotation between frames
- Use of quaternions to describe rotations

Euler angles, commonly known as *roll-pitch-yaw* (φ, θ, ψ) describe three independent rotations of a body frame with respect to an inertial frame. These rotations are respectively about the x,y and z axes. Furthermore a given body attitude can be described as a rotation matrix with respect to the referred Euler angles. Despite being probably the most intuitive method, there's an issue regarding Euler angles. Euler kinematic equations may become singular[1] for some angle sequences, this problem is commonly know as *gimball lock*. Hence, this method is not suitable for the attitude control problem, since satellite attitude is not confined to a given angle interval.

The second method describes an attitude using a single rotation vector. An important Euler's theorem states that any rotation between two frames can be described according to a single axis rotation, denoted as *Euler axis*. Knowing the initial and target satellite orientations it is possible to compute the respective *Euler axis* and its corresponding principal angle, see Appendix C for further details. Although having the advantage of minimizing the angular motion path, the computation of the corresponding rotation matrix can be computationally cost demanding since it requires to compute at least six *error attitude matrix* elements at every instant of time, see [16].

Quaternion notation describes the satellite attitude also taking advantage of *Euler axis* theorem. Although, when compared to *Euler axis* rotation matrix method, it has the benefit of requiring only four components to describe the satellite attitude. Moreover it doesn't contain any singularities. Thus, quaternions are suitable for describing satellite attitudes.

3.1.2 Quaternion attitude description

This subsection describes a simple satellite attitude control law according to quaternion notation.

A satellite attitude closed-loop control scheme using quaternion notation requires an attitude error matrix computation (3.3). Since quaternions can be related to a general rotation matrix, see (C.20), the attitude error matrix (3.3) can easily be written with respect to quaternions.

Let q_t be the target orientation and q_s be the current satellite orientation, both written in quaternion terminology. Therefore the attitude error matrix in quaternion notation can be defined as a quaternion multiplication, described in (3.4) , see (C.23) for further details .

$$[A(q_e)] = [A(q_t)].[A(q_s)]^{-1} = [A(q_t)][A(q_s^{-1})] \tag{3.4}$$

[1] A kinematic singularity is a point within the robot's or device motion workspace where its *Jacobian* matrix loses rank.

Expanding (3.4) with respect to quaternion components yields,

$$q_t.q_s^{-1} = q_e = \begin{bmatrix} q_{t4} & q_{t3} & -q_{t2} & -q_{t1} \\ -q_{t3} & q_{t4} & q_{t1} & -q_{t2} \\ q_{t2} & -q_{t1} & q_{t4} & -q_{t3} \\ q_{t1} & q_{t2} & q_{t3} & q_{t4} \end{bmatrix} \begin{bmatrix} q_{s1} \\ q_{s2} \\ q_{s3} \\ q_{s4} \end{bmatrix} \tag{3.5}$$

where q_e denotes the satellite error quaternion.

The satellite control law can be obtained considering the following relations between quaternion components and direction cosine matrix components,

$$\begin{aligned} q_4 &= \pm\tfrac{1}{2}\sqrt{1 + a_{11} + a_{22} + a_{33}} \\ q_1 &= \tfrac{1}{4}(a_{23} - a_{32})/q_4 \\ q_2 &= \tfrac{1}{4}(a_{31} - a_{13})/q_4 \\ q_3 &= \tfrac{1}{4}(a_{12} - a_{21})/q_4 \end{aligned} \tag{3.6}$$

Hence, making $g_e = [q_{e1}q_{e2}q_{e3}]^T$ components equal to zero, both the target and the satellite frames coincide. Therefore, a valid simple control law is given by a simple proportional derivative controller, see (3.7).

$$\begin{aligned} \tau_{cx} &= 2K_x q_{e1} q_{e4} + K_{dx}\omega_x \\ \tau_{cy} &= 2K_y q_{e2} q_{e4} + K_{dy}\omega_y \\ \tau_{cz} &= 2K_z q_{e3} q_{e4} + K_{dz}\omega_z \end{aligned} \tag{3.7}$$

The control law (3.7) will be considered for a SACS model described in Section 3.1.4.

3.1.3 Non-linear Model equations

Non-linear satellite dynamical model equations are obtained according to Euler's equations, see Appendix A.1.3 for a general Euler's equations computation. Due to computational benefits, satellite dynamical models are usually based upon quaternion terminology. See [4] for a similar SACS problem approach, additionally another satellite attitude control scheme based in quaternions is described in [16].

Assuming no external torques, the satellite system dynamics is described as (3.8), see (A.26) for further details.

$$\dot{h}_I = \dot{h}_B - \omega \times h_B \tag{3.8}$$

where h_I and h_B denote respectively the overall satellite system angular momentum with respect to an inertial frame and the angular momentum described with respect to the satellite frame.

Let the satellite system dynamic equations be written with respect to the inertial frame. Consider that $\tau = \tau_s + \tau_{RTD}$ and $h = h_s + h_{RTD}$ refer respectively to torque and angular momentum sums of the satellite and RTD. If external torques exist, they have to be accounted for, i.e. $\tau_s + \tau_{RTD} = \tau_{ext}$, otherwise the torque and angular momentum sums of the satellite and RTD equal zero.

Therefore the satellite dynamics general equation yields,

$$\frac{d}{dt}(J_s\,\omega) + \dot{h}_{RTD} = \tau_{ext} - \omega \times (J_s\,\omega) - \omega \times h_{RTD} \tag{3.9}$$

where, τ_{ext} denotes the total external torque. This can be written equivalently as,

$$\dot{\omega} = J_s^{-1}\,\omega \times (J_s\,\omega) - J_s^{-1}(\omega \times h_{RTD}) - J_s^{-1}\,\dot{h}_{RTD} + J_s^{-1}\,\tau_{ext} \tag{3.10}$$

Matrix $S(\omega)$, see A.17, simplifies the angular velocity cross product in (3.10), thus (3.10) can be written as,

$$\dot{\omega} = J_s^{-1}\,S(\omega)\,J_s\,\omega - J_s^{-1}\,S(\omega)\,h_{RTD} - J_s^{-1}\tau_{ctrl} + J_s^{-1}\,\tau_{ext} \tag{3.11}$$

Note that $\dot{h}_{RTD}$ is assumed to be equivalent to τ_{ctrl}.

Since satellite attitude is described with respect to quaternion notation, consider the quaternion time derivative (3.12), see Appendix C for further details.

$$\dot{q} = \frac{1}{2}[\Omega(\omega)]q \tag{3.12}$$

The satellite plant block diagram in Figure 3.2, describes the satellite behaviour according to (3.11). This block diagram can be used in a Simulink® model for simulation purposes. Hence, the satellite plant receives control torques as inputs which are generated from a given RTD. Consequently RTDs must be analysed in order to characterize its composing components motion, see Section 3.2.

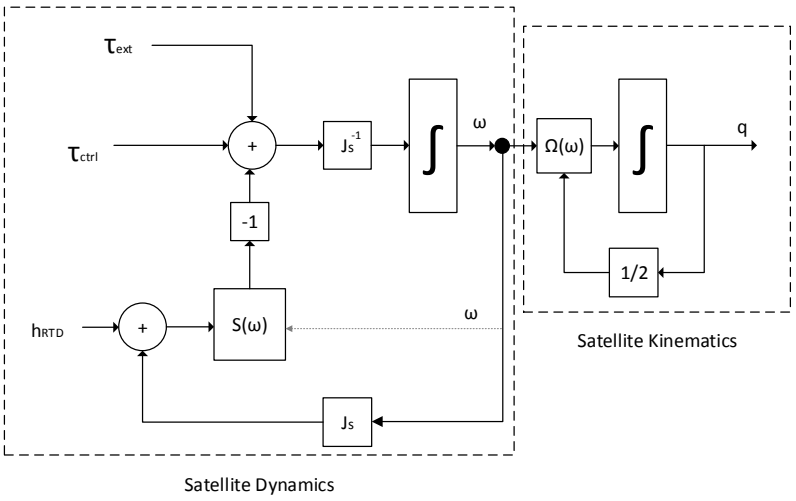

Figure 3.2: Satellite plant block diagram

3.1.4 Attitude control closed loop

The concepts introduced in the last three subsections describe a satellite attitude dynamic model. Furthermore, satellite target attitude tracking can be ensured by a simple feedback control scheme.

Chapter 4 considers a generic *PD* control law (3.7) ensuring the satellite attitude convergence to any attitude references. Figure 3.3 illustrates a satellite attitude feedback control scheme based upon control law (3.7).

Considering a reference quaternion vector, q_{ref} as control scheme input, the quaternion error, q_e can be computed according to (3.5). In fact, *"Error quaternion computation"* block illustrated in Figure 3.3 performs the computations described by (3.5) and ensures the satellite Euler axis angular trajectory tracking. Consequently the quaternion error vector q_e is fed to the controller in order to compute the RTD requested output torque. The command control u is given to the *"Reaction Torque Device"* block, where all computations regarding RTD components motion are performed.

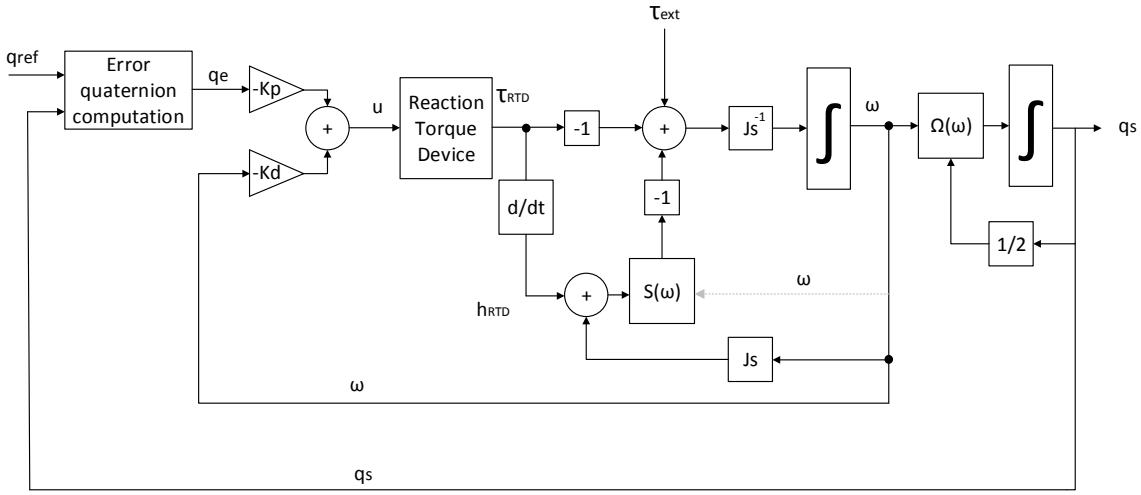

Figure 3.3: Attitude control loop

This Section defined the required satellite model framework enabling the RSA performance analysis. Section 3.2 describes both the RSA components motion and a RW arrangement. The characterization of these two devices allows their inclusion into the satellite model enabling their performance comparison.

3.2 Reaction torque device systems

3.2.1 RSA device

Now that the RSA feasibility is proved it is required to compute the RSA output torque relation with its composing components motion, i.e its internal sphere and actuators motion must be characterized. The following analysis is conducted for an actuator system according to a regular tetrahedral geometry. Nevertheless, the following expressions can be adjusted to other actuation system configurations. First, it is required to verify if the adopted geometry guarantees the system static equilibrium.

Consider a RSA actuator system composed of four holonomic actuators having their contact points over the sphere surface according to a regular tetrahedron vertices circumscribed in the sphere, see Figure 3.4.

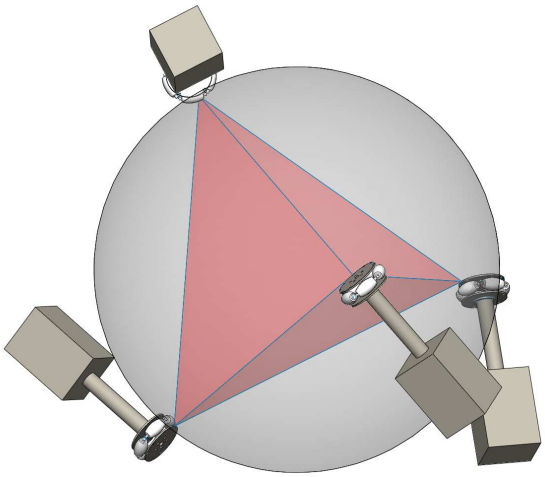

Figure 3.4: Regular Tetrahedral geometry with actuator systeme

Since the RSA concept requires a internal sphere with three independent rotational DOF, the sphere geometrical center must be static with respect to an inertial frame in the RSA outer shell, when the actuators contact is imposed. The static equilibrium can be verified considering to the following equations,

$$\begin{aligned} \textstyle\sum_i^n F_i = 0 \\ \textstyle\sum_i^n \tau_i = 0 \end{aligned} \tag{3.13}$$

where F_i and τ_i denote respectively all the system forces and momenta. The static equilibrium proof with $n = 4$ actuators disposed according to a regular tetrahedral geometry is described in Appendix B.1.

There are multiple actuators rotational vectors combinations that verify the RSA sphere static equilibrium. Thus, a possible one is described as,

$$\begin{bmatrix} \omega_{1x} \\ \omega_{1y} \\ \omega_{1z} \end{bmatrix} = \begin{bmatrix} \frac{1}{2} - \frac{\sqrt{3}}{6} \\ \frac{\sqrt{3}}{6} + \frac{1}{2} \\ \frac{-\sqrt{3}}{3} \end{bmatrix}, \begin{bmatrix} \omega_{2x} \\ \omega_{2y} \\ \omega_{2z} \end{bmatrix} = \begin{bmatrix} \frac{-\sqrt{3}}{6} - \frac{1}{2} \\ \frac{1}{2} - \frac{\sqrt{3}}{6} \\ \frac{\sqrt{3}}{3} \end{bmatrix}, \begin{bmatrix} \omega_{3x} \\ \omega_{3y} \\ \omega_{3z} \end{bmatrix} = \begin{bmatrix} \frac{\sqrt{3}}{6} - \frac{1}{2} \\ \frac{\sqrt{3}}{6} - \frac{1}{2} \\ \frac{-\sqrt{3}}{3} \end{bmatrix}, \begin{bmatrix} \omega_{4x} \\ \omega_{4y} \\ \omega_{4z} \end{bmatrix} = \begin{bmatrix} \frac{\sqrt{3}}{6} + \frac{1}{2} \\ \frac{\sqrt{3}}{6} - \frac{1}{2} \\ \frac{\sqrt{3}}{3} \end{bmatrix} \tag{3.14}$$

For further details regarding the actuators hub axes vectors computation see Appendix B.2.

Figure 3.5 shows the adopted axes convention for each actuator reference frame. The wheel hub axis or rotational axis corresponds to frame x axis, whereas the slip axis corresponds to y axis. The following RSA analysis assumes the use of holonomic Swedish wheels with $\gamma = \frac{\pi}{2}$, see Section 2.3. Hence the computation of four actuator reference frames allows the determination of their corresponding transformation matrices with respect to the sphere reference frame.

Figure 3.6 illustrates four actuators reference frames according to a regular tetrahedral geometry. Additionally the sphere reference frame is also depicted in magenta. Each actuator frame is defined by three axis, the hub axis (blue), the slip axis (red) and the normal contact vector axis (green). Let's assume that the sphere reference frame doesn't follow the sphere motion and their axes remain static with respect to an inertial frame defined in the RSA outer shell. Let's assume static actuators for the present

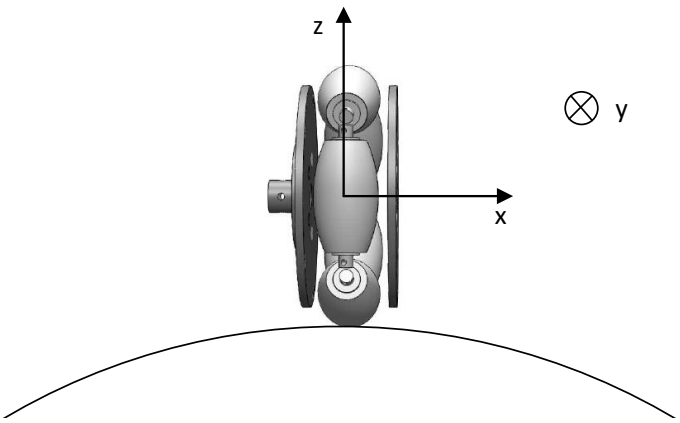

Figure 3.5: Actuator Reference Frame

analysis, i.e. their contact points location are invariant with respect to the sphere frame. Furthermore [19] performs a similar characterization of a sphere in mechanical contact with holonomic wheels.

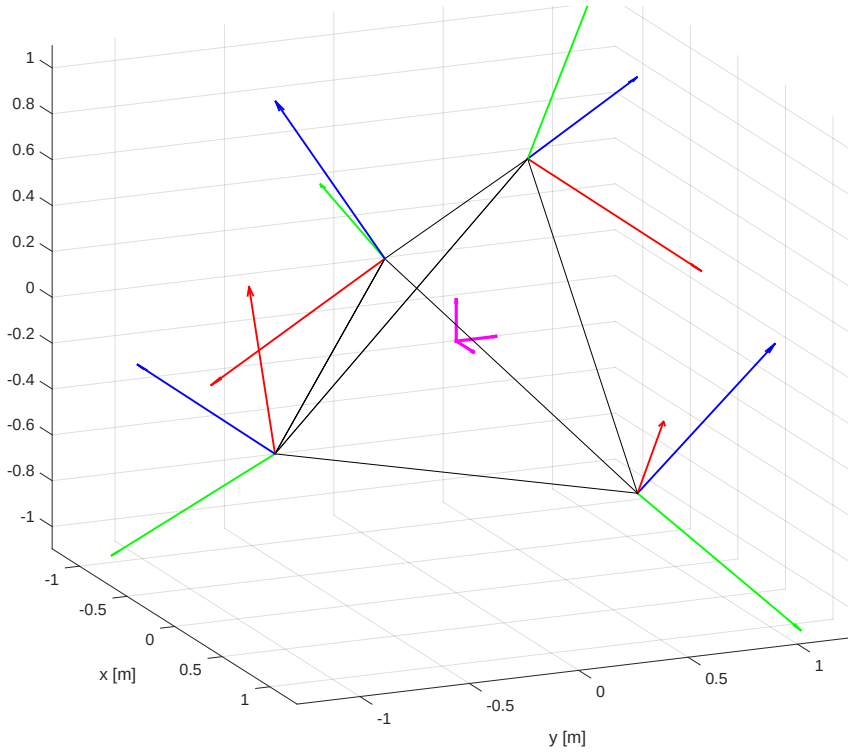

Figure 3.6: Tetrahedral Actuator Reference Frames

Note that the following geometric vectors computations are all described with respect to the sphere reference frame.

Let p_i be actuator i contact point location and Ω_s be the sphere angular velocity. For a given sphere rotational motion, there's an unique corresponding tangential velocity in the contact point between the actuator i and sphere surface. This contact point tangential velocity can be determined as follows,

$$V_i = \Omega_s \times p_i \tag{3.15}$$

For holonomic wheel actuators, the contact point tangential velocity can be decomposed in two actuator velocity components, namely the hub axis and slip axis components. Therefore, V_i can be written as follows,

$$V_i = V_{i\ hub} \cdot \hat{v}_{i\ hub} + V_{i\ slip} \cdot \hat{v}_{i\ slip} \tag{3.16}$$

where, $\hat{v}_{i\ hub}$ and $\hat{v}_{i\ slip}$ denote respectively the actuator hub axis and slip axis unit vectors, whereas $V_{i\ hub}$ and $V_{i\ slip}$ refer respectively to their magnitudes. The following model assumes a no-slip situation where the contact point tangential velocity between the actuator and sphere surface is equivalent both in the sphere frame and the actuator frame. This assumption can be easily defined as,

$$(\Omega_s \times p_i) \cdot \hat{v}_{i\ hub} = V_{i\ hub} \tag{3.17}$$

Cross product properties let (3.17) be written equivalently as,

$$(p_i \times \hat{v}_{i\ hub}) \cdot \Omega_s = V_{i\ hub} \tag{3.18}$$

Since all actuators contact points lie in the sphere surface, their contact position vector norm is equivalent to the sphere radius, denoted as R_s. Thus, $p_i = R_s\, \hat{p}_i$, where $\hat{p}_i$ is the actuator i contact point unit vector, thus (3.17) yields,

$$(\hat{p}_i \times \hat{v}_{i\ hub}) \cdot \Omega_s = \frac{V_{i\ hub}}{R_s} \tag{3.19}$$

The sphere rotational motion can be described with respect to the actuator rotational motion, thus consider the relation between the actuator contact point tangential velocity and the actuator rotational velocity (3.20).

$$V_{i\ hub} = \omega_i R_w \tag{3.20}$$

where, ω_i and R_w refer respectively to the actuator angular velocity and the actuator wheel radius. Substituting (3.20) in (3.18) yields,

$$(\hat{p}_i \times \hat{v}_{i\ hub}) \cdot \Omega_s = \frac{\omega_i}{R_s} R_w \tag{3.21}$$

Considering actuator i hub axis rotational unit vector ($\hat{p}_i \times \hat{v}_{i\ hub}$ as $\hat{\mathsf{w}}_i$), (3.21) can be expanded for three actuators as follows,

$$\begin{bmatrix} \hat{\mathsf{w}}_1^T \\ \hat{\mathsf{w}}_2^T \\ \hat{\mathsf{w}}_3^T \end{bmatrix} \Omega_s = k \begin{bmatrix} \omega_1 \\ \omega_2 \\ \omega_3 \end{bmatrix} \tag{3.22}$$

where, k denotes the transmission gear ration defined as $k = \frac{R_w}{R_s}$.

$$\mathsf{W} = \begin{bmatrix} \hat{\mathsf{w}}_1 \hat{\mathsf{w}}_2 \hat{\mathsf{w}}_3 \end{bmatrix} \tag{3.23}$$

Matrix (3.23) will be referred as the distribution matrix, describing how the sphere angular motion is converted with respect to each actuator frame. Hence, the actuators angular velocity can be computed

according to,

$$\begin{bmatrix} \omega_1 \\ \omega_2 \\ \omega_3 \end{bmatrix} = \frac{1}{k} \underbrace{\begin{bmatrix} \hat{\mathbf{w}}_{1x} & \hat{\mathbf{w}}_{1y} & \hat{\mathbf{w}}_{1z} \\ \hat{\mathbf{w}}_{2x} & \hat{\mathbf{w}}_{2y} & \hat{\mathbf{w}}_{2z} \\ \hat{\mathbf{w}}_{3x} & \hat{\mathbf{w}}_{3y} & \hat{\mathbf{w}}_{3z} \end{bmatrix}}_{\mathsf{W}^T} \begin{bmatrix} \Omega_x \\ \Omega_y \\ \Omega_z \end{bmatrix} \tag{3.24}$$

Note that, similarly to distribution matrix W^T an analogous matrix for the actuators slip axis can be computed.

There's now sufficient information to define the system *Jacobian* [2]. For the present case, the sphere motion corresponds to the end-effector. Hence the *Jacobian* (denoted as J) is depicted in (3.25).

$$\Omega = \underbrace{k \left[\mathsf{W}^T\right]^{-1}}_{\mathsf{J}} \begin{bmatrix} \omega_1 \\ \omega_2 \\ \omega_3 \end{bmatrix} \tag{3.25}$$

The *Jacobian* has the property of being time-invariant, since it only relies on the system constants (i.e. the actuators position coordinates and ratio k). Therefore, it can also be used for angular acceleration terms, see (3.26).

$$\dot{\Omega} = \mathsf{J}\dot{\omega} \tag{3.26}$$

Furthermore, the RSA *Jacobian* can be also used to relate the sphere and actuators torques. Note that the conversion from torques to angular acceleration depends upon the constant body inertia tensor (which is usually constant), see (A.22) for further details.

The sphere torque τ_s is obtained from a linear combination of actuators torque coefficients τ_{wi} multiplied by their respective actuator hub axis unit vectors. Hence in matrix form, this follows as,

$$\tau_s = \mathsf{J}\tau_w \tag{3.27}$$

Furthermore, the inverse Jacobian (3.28) relates the sphere angular motion with the actuators angular motion.

$$J^{-1} = \frac{1}{k}\mathsf{W}^T \tag{3.28}$$

For $n > 3$ actuators, matrix W^T is no longer a 3×3 square matrix and therefore its normal inverse is not feasible, having implications regarding the *Jacobian* computation. Nevertheless, non-squared matrices inverses can be computed according to pseudoinverse methods. The most common is known as the Moore-Penrose pseudoinverse. Thus, the RSA *Jacobian* computation is feasible for $n > 3$ actuators, e.g. an actuator system according to a regular tetrahedral configuration.

An important property regarding this RSA geometry *Jacobian* concerns the fact of it being singularity free, when W^T matrix is full rank. Thus a RSA with an actuator system according to a regular tetrahedral configuration can induce any angular motion to the RSA internal sphere.

[2] By definition, the *Jacobian* matrix relates the joint coordinates motion variations with the end-effector coordinates motion.

The RSA *Jacobian* also shows that a sphere motion results in an unique motion for all actuators in mechanical contact with its surface, see (3.24), thus implying that actuators motion must be synchronized. Such imposition has consequences for the motors actuating the holonomic wheels. Moreover such motor motion dependencies must be accounted for motor models. Appendix E shows a brief analysis regarding a simple DC motor model.

Implementing DC motor models in a simulation environment requires their adjustment to the load physical properties, such as gear ratios and load inertia reflected in the motor frame. Furthermore, each motor model must account for the torque that all other motors perform at each instant in its frame. Such computation can be performed considering all motors transformation matrices with respect to each other, thus each motor torque should be described in every motor frame at every instant. Consequently at every time instant each motor sees a load torque, τ_L, see Figure E.2, corresponding to the torque sum that all remaining motors perform in its frame. These motor torques frame transformations can also be seen as simple torque projections upon each motor rotational axis. This effect is commonly known as motor "load sharing" describing the cooperation between motors to achieve the desired sphere torque. Consequently when a RSA with more actuators is considered, the total actuator motors energy will be approximately equal differing only in how the load/energy is shared over all motors.

3.2.2 Reaction wheels arrangement device

RW arrangements are commonly used in satellites to produce reaction torques. A RW arrangement comprises a set of n RWs composed of an inertia disk actuated by an electrical motor. One important feature that distinguishes RWs devices from a RSA device, refers to the possibility of controlling each RW independently.

The torque produced by each RW is applied to the satellite frame according to its hub axis vector. Note that since RWs torques are independent, the overall torque applied to the satellite is given by the sum of all the RWs torque vectors. Hence, assuming that a RW i has its hub axis unit vector defined as $\hat{\mathsf{w}}_{rwi}$, the overall control torque applied to the satellite is obtained according to (3.29).

$$\tau_{ctrl} = \underbrace{\begin{bmatrix} \hat{\mathsf{w}}_{rw1} & \hat{\mathsf{w}}_{rw2} & \cdots & \hat{\mathsf{w}}_{rwn} \end{bmatrix}}_{\mathsf{W}_{rw}} \underbrace{\begin{bmatrix} \tau_{rw1} \\ \tau_{rw2} \\ \vdots \\ \tau_{rwn} \end{bmatrix}}_{\tau_{rw}} \tag{3.29}$$

where τ_{rw} and τ_{ctrl} refer respectively to RWs torque coefficients and control torque applied to the satellite. Therefore, the W_{rw} distribution matrix (dimension $3 \times n$) relates the RWs torques with the control torque applied to the satellite. The following expressions assume the RWs hub axis unit vectors, $\hat{\mathsf{w}}_{rwi}$ to be all non coplanar with respect to each other.

For RWs arragements composed of three RWs, matrix W_{rw} has 3×3 dimension and is full rank, meaning that the problem solution is uniquely defined. Consequently matrix W_{rw} has a well defined

inverse matrix, see (3.30).

$$\begin{bmatrix} \tau_{rw1} \\ \tau_{rw2} \\ \tau_{rw3} \end{bmatrix} = \mathsf{W}_{rw}^{-1}.\tau_{ctrl} \tag{3.30}$$

For redundant RWs arrangements the problem is no longer uniquely defined, since matrix W_{rw} is no longer a square matrix. Consequently a optimal criterion is required to choose between one among all RWs torque combinations for a given control torque vector.

There are mainly two optimal criteria adopted to find RWs arrangements solutions, they are based upon the Euclidean norm (L_2) and the Frobenius norm (L_∞) optimization. The Euclidean norm optimization is addressed via the Moore-Penrose pseudoinverse, whereas the Frobenius norm optimization is addressed via a torque envelop minmax problem, see [23] for a detailed analysis.

For energy comparison purposes, the L_2 optimization attains better results, see [23]. Hence, in chapter 4 only this optimization method is considered. For further details regarding RWs torque distribution with respect to Moore-Penrose pseudoinverse see Appendix D.

This Section defined the equations characterizing both RTDs dynamics, which are considered in Chapter 4. Hence, if a Simulink® environment is used for simulations purposes, the RTD block should include the respective RTD dynamics (e.g. Jacobian and motor dynamics).

Chapter 4

Results

This chapter analyses the results for a satellite attitude dynamical Simulink® model.

Section 4.1 shows the satellite attitude control scheme maneuvering neglecting RTDs. In other words, this means that the control torque computed by the PD control law is directly applied to the satellite frame. Therefore, verifying a set of attitude references simulations the SACS attitude reference tracking convergence can be analysed.

Section 4.2 shows a Simulink® SACS model with a RTD inclusion in order to describe reaction torque generation. Furthermore the RTDs components motion description, enables an energy consumption comparison of both RTDs, namely a RSA and a RW arrangement. There are several RTDs valid configurations varying in actuators number, geometry and physical parameters. Therefore, to allow a general analysis for both RTDs performance, an approach considering some RSA and RW arrangements configurations is performed. Comparing both RTDs having equivalent physical parameters (equivalent mass and volume) it is possible to show the RSA benefits compared to RW arrangements .

The models used in this chapter neglect systems losses, disturbances and uncertainties, i.e. parameters such as friction coefficients, slippage in mechanical rolling contact, attitude estimation uncertainties and others. Consequently, this Chapter goal is to compare both RTDs performance from a general point of view allowing to state valid conclusions regarding their ideal performance. Nevertheless, Section 4.3 depicts some negative factors affecting both the satellite and RTDs, which cannot be neglected in a real world environment.

4.1 Satellite attitude control scheme without a RTD

SACS Simulink® model validation concerns a serie of satellite attitude maneuverings simulations in order to verify the SACS dynamics and control strategy performance.

Satellite target attitude is described according to Euler angles (φ, θ, ψ), due to their ease in visual attitude perception. Nevertheless, SACS computes the satellite attitude based upon quaternion notation. Figure 4.1 illustrates the SACS Simulink® model without a RTD block between the PD controller and satellite plant.

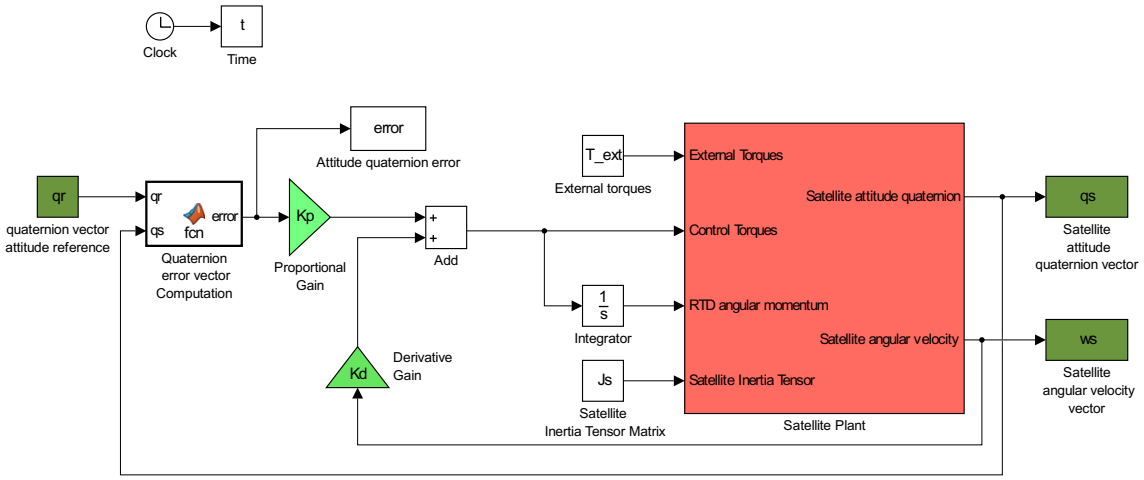

Figure 4.1: Simulink® Model

SACS Simulink® model simulation requires some satellite plant physical parameters definition, see Table 4.1.

Table 4.1: SACS model without RTD simulation parameters

Parameter	Value (*SI* units)
Satellite Inertia Tensor Matrix $[Kg\ m^2]$	$\begin{bmatrix} 2 & 0 & 0 \\ 0 & 2 & 0 \\ 0 & 0 & 2 \end{bmatrix}$
External Torque vector $[Nm]$	$\begin{bmatrix} 0 & 0 & 0 \end{bmatrix}^T$
Satellite initial attitude quaternion	$\begin{bmatrix} 0 & 0 & 0 & 1 \end{bmatrix}^T$
Satellite initial angular velocity $[rads^{-1}]$	$\begin{bmatrix} 0 & 0 & 0 \end{bmatrix}^T$
Satellite initial angular momentum $[Nms]$	$\begin{bmatrix} 0 & 0 & 0 \end{bmatrix}^T$
Proportional Gain	$K_p = -2$
Derivative Gain	$K_d = -2$

Consider a satellite attitude maneuvering simulation for a z axis (yaw) rotation of $\psi = \frac{\pi}{4}$, illustrated in Figure 4.2, where Figure 4.3 shows the respective satellite convergence to the reference attitude. In fact, the satellite attitude converges to the desired quaternion attitude, $q_r = \begin{bmatrix} 0 & 0 & 0.3827 & 0.9239 \end{bmatrix}$, with a settling time of approximately $t_s = 12.3s$. Moreover the SACS settling time is determined by the satellite control gains. Consider the same $\psi = \frac{\pi}{4}$ rotation, where proportional and derivative controller gains have been increased to $K_p = -4$ and $K_d = -4$ in order to denote the satellite settling time decrease. Figure 4.4 shows the referred SACS simulation results denoting the referred settling time decrease to $t_s = 5.0s$. Note that, the SACS settling time and dynamic response also varies according to other parameters, such as the satellite inertia tensor, the satellite initial parameters and external disturbances. Figures 4.5, 4.6 and 4.7 show the SACS convergence for distinct references attitudes. Despite being non intuitive to analyse a graph with more than one angular velocity components, the angular velocity components sum

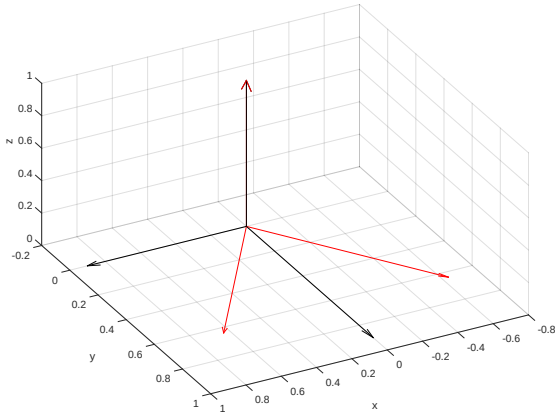

Figure 4.2: Yaw rotation of $\psi = \frac{\pi}{4}$

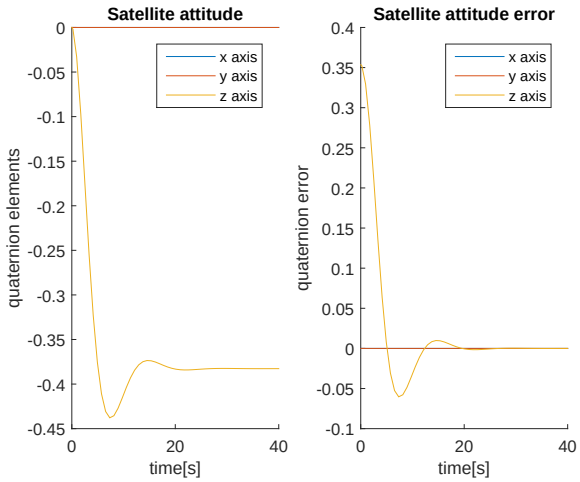

Figure 4.3: Yaw rotation of $\psi = \frac{\pi}{4}$ SACS simulation (with $K_p = K_d = -2$)

corresponds to the Euler axis, which ensures the minimum angular path performed by the satellite, see Appendix C.

The previous results illustrate the SACS convergence for some reference attitudes, in fact, this convergence is verified for any other reference attitudes. Hence since SACS is well behaved let us consider a RTD inclusion into the SACS, see Section 4.2.

4.2 RTDs comparison for a satellite attitude control scheme

This Section illustrates a SACS Simulink ® model concerning two distinct RTDs, namely a RSA and a RW arrangement. The performance attained by each RTD depends upon their physical parameters, thus in order to state a valid comparison, their physical parameters must be equivalent. In other words, their physical mass and dimensions must be equivalent. This assumption allows a general RTD performance

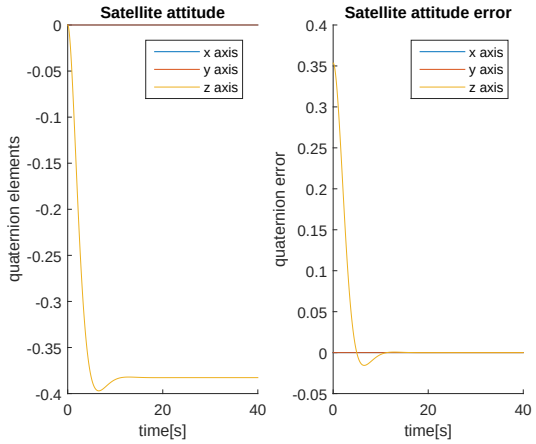

Figure 4.4: Yaw rotation of $\psi = \frac{\pi}{4}$ SACS simulation (with $K_p = K_d = -4$)

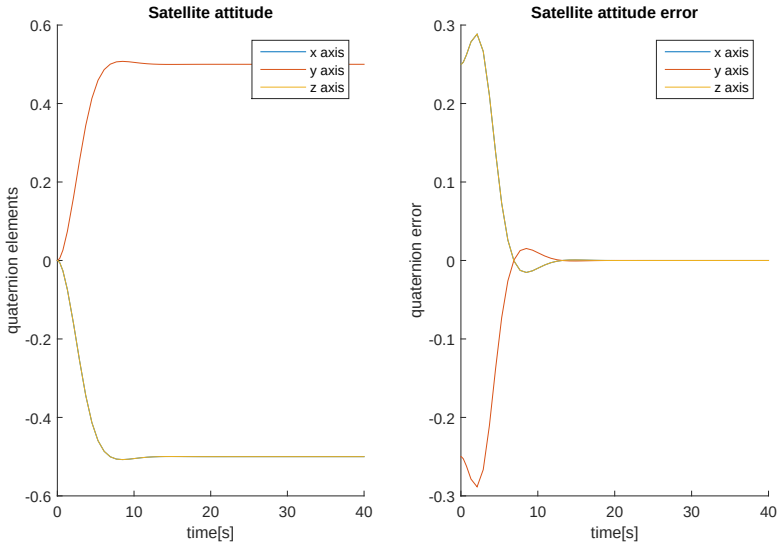

Figure 4.5: Rotation of $[\varphi = \frac{\pi}{2}, \theta = -\frac{\pi}{2}, \psi = 0]$ SACS simulation (with $K_p = -2$ and $K_d = -2$)

comparison regarding only the actuators geometry benefits and neglecting losses or disturbances.

The comparison of both RTDs requires the choice of a given performance measurement metric. Consequently consider both devices energy consumption measurement, allowing to state valid conclusions about their performances. Equivalently changing RTDs physical parameters and setting an energy consumption limit would result in the same conclusion, although instead of being in energy units it would be with respect to mass, volume or other physical parameter.

For simplicity and allowing the results to be the most general possible, the energy spent by each RTD is described with respect to the mechanical work done by each RTD composing rigid bodies. Concerning the RSA, let the mechanical work performed by the sphere be the RSA energy measurement. Whereas for a RW arrangement let the sum of the mechanical work performed by each RW rotating disk be the

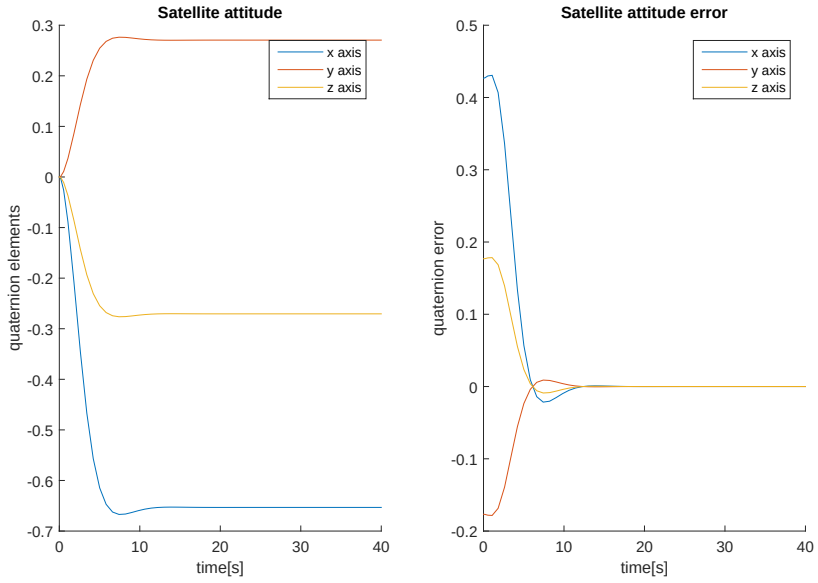

Figure 4.6: Rotation of $[\varphi = \frac{\pi}{2}, \theta = -\frac{\pi}{4}, \psi = 0]$ SACS simulation (with $K_p = -2$ and $K_d = -2$)

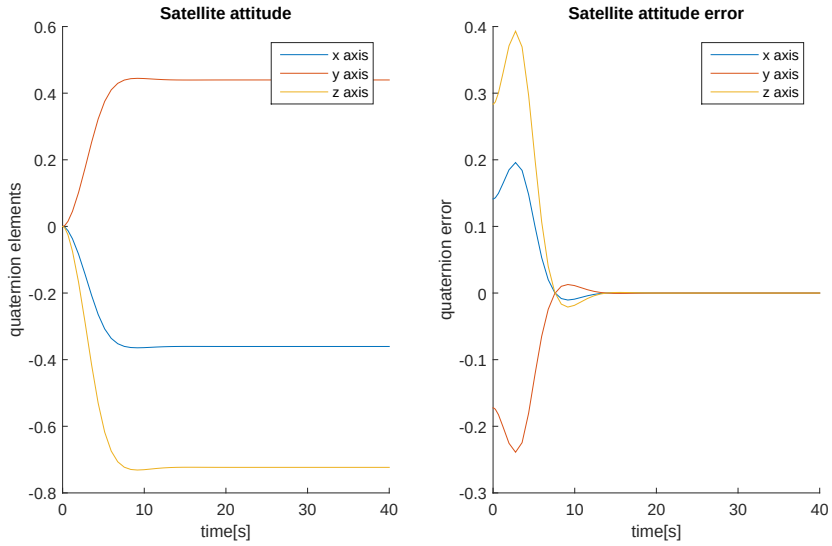

Figure 4.7: Rotation of $[\varphi = \frac{7\pi}{4}, \theta = -\frac{7\pi}{3}, \psi = \frac{5\pi}{6}]$ SACS simulation (with $K_p = -2$ and $K_d = -2$)

RW arrangement energy measurement. This work-energy equivalent analysis follows the Work-Energy principle, see [8] for a Work-Energy principle definition.

The mechanical work of a rigid body in rotational motion is given as,

$$W = \tau\theta \tag{4.1}$$

where, θ denotes the rigid body angular displacement. Equivalently one can consider the mechanical power at each time instant and compute its time integral. Consequently, the mechanical power for rotational motion is given by,

$$\frac{d}{dt}W = \tau\omega \tag{4.2}$$

Comparing the mechanical work expended by both RTD's angular motions, it is possible to state which one is more efficient in energy terms. Furthermore in an ideal situation the RTD energy would correspond to actuators motor energy, verifying (4.3). This means that the DC motors power applied to the inertia load (rotating bodies) would be totally converted into mechanical power.

$$P_{motors} = P_m \tag{4.3}$$

The present SACS includes a motor dynamics block, which can determine the rigid bodies angular motion transient responses, see Appendix E for further details. Nevertheless the following simulations don't account for such responses since they would not have considerable impact upon the mechanical work result.

The valid comparison of both RTDs implemented in a SACS requires the definition of the overall simulation parameters. Furthermore RTDs physical parameters must be equivalent as referred above. Henceforth Table 4.2 states SACS Simulink ® model simulation parameters. Note that hollow bodies are considered for both RTDs since they allow higher inertia moments. The RTD's components mass and dimension have a critical impact in both RTDs performance measurement. Therefore, it is assumed that both RTDs have equivalent masses and volumes.

Table 4.2: SACS model simulation parameters

Parameter	Value (*SI* units)
Satellite Inertia Tensor Matrix $[Kg\ m^2]$	$\begin{bmatrix} 3 & 0 & 0 \\ 0 & 3 & 0 \\ 0 & 0 & 3 \end{bmatrix}$
External Torque vector $[Nm]$	$\begin{bmatrix} 0 & 0 & 0 \end{bmatrix}^T$
Satellite initial attitude quaternion	$\begin{bmatrix} 0 & 0 & 0 & 1 \end{bmatrix}^T$
Satellite initial angular velocity $[rads^{-1}]$	$\begin{bmatrix} 0 & 0 & 0 \end{bmatrix}^T$
Satellite initial angular momentum $[Nms]$	$\begin{bmatrix} 0 & 0 & 0 \end{bmatrix}^T$
Proportional Gain	$K_p = -5$
Derivative Gain	$K_d = -5$
Hollow Sphere Mass $[Kg]$	1
Hollow Sphere outer Radius $[m]$	0.1
Hollow Sphere inner Radius $[m]$	0.09
Hollow Disk Mass $[Kg]$	$\frac{1}{3}$
Hollow Disk outer Radius $[m]$	0.1
Hollow Disk inner Radius $[m]$	0.09
Hollow Disk Height $[m]$	0.1

The simulations concerning distinct RTDs require distinct Simulink® models, although here only the SACS Simulink ® model with RSA is illustrated, see Figure 4.8. Nevertheless it can be seen that both RSA and RW arrangement blocks are similar, see Section 4.2 for further details. Considering Figure

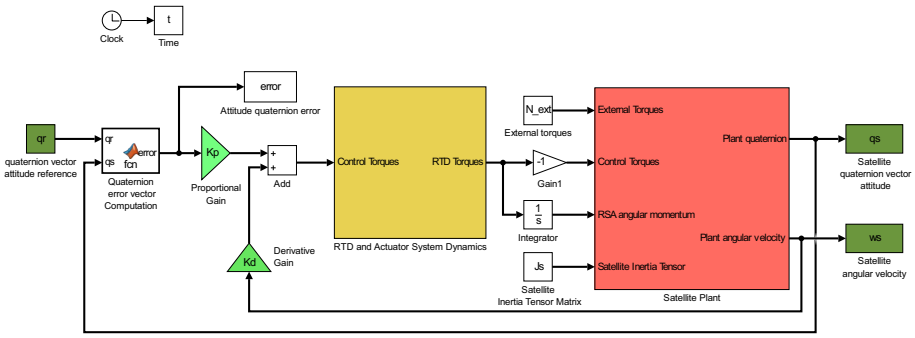

Figure 4.8: SACS model with RTD

4.8 model, the RTD block receives a torque vector computed by the PD control law according to the quaternion error and converts it into the sphere actuator wheels frames. This conversion is performed according to the RSA Jacobian, see (3.26).

Figure 4.9 shows the RSA block (RTD block) concerning four actuators. Moreover, angular accelerations are obtained by multiplying the control torques by the RSA sphere inertia tensor (J_{sphere}). Consequently the RSA *Jacobian* computes the actuators angular motions. Alternatively the RSA *Jacobian* can be also used to find the actuators torques, see Section 3.2. Furthermore in an ideal situation, any actuator angular motion can be fulfilled, although in a real case such motions are constrained by several parameters such as, motor physical limitations, slip occurrence and others. Note that such parameters could be considered in motor dynamics block.

Since this thesis aims to show a general result, an ideal situation is considered, thus not making use of the motors dynamics or other losses. A similar procedure occurs for the RTD block characterizing RW arrangements.

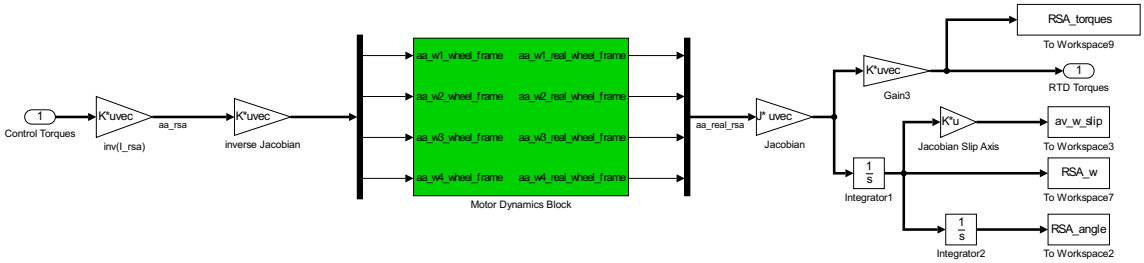

Figure 4.9: RTD block

The following SACS Simulink ® model simulations assume the following RTDs conditions,

- The total RW arrangement mass equals the RSA sphere mass.
- Each RW radius is equivalent to the sphere radius.
- Both RSA and RWs are hollow in order to increase its moment of inertia for a given mass, therefore both bodies have inner and outer radius referred as r_{in} and r_{out}.

Let the RSA be composed of a $10\ cm$ radius sphere with $1\ Kg$ mass and shell cross section thickness of $1\ cm$. Therefore an equivalent RW arrangement would be composed of three disks each with $10\ cm$

radius, cross section thickness $1\ cm$ and mass equal to $\frac{1}{3}\ Kg$. The RW disk height does not affect the reaction torque outcome, therefore it would be equal to $\frac{1}{3}$ of the sphere radius allowing a total volume equivalence, see (4.5). Consequently, a four RW arrangement would have $\frac{1}{4}\ Kg$ mass for each RW.

Furthermore, both generic RTD's inertia tensors yield,

$$J_s = \begin{bmatrix} \frac{2}{5}\cdot m_s \cdot \frac{r^5_{s(out)} - r^5_{s(in)}}{r^3_{s(out)} - r^3_{s(in)}} & 0 & 0 \\ 0 & \frac{2}{5}\cdot m_s \cdot \frac{r^5_{s(out)} - r^5_{s(in)}}{r^3_{s(out)} - r^3_{s(in)}} & 0 \\ 0 & 0 & \frac{2}{5}\cdot m_s \cdot \frac{r^5_{s(out)} - r^5_{s(in)}}{r^3_{s(out)} - r^3_{s(in)}} \end{bmatrix} \tag{4.4}$$

Matrices (4.4) and (4.5) show that a hollow sphere has larger moments of inertia assuming a mass equivalence.

$$J_w = \begin{bmatrix} \frac{1}{2}\cdot m_w \cdot (r^2_{w(out)} + r^2_{w(in)}) & 0 & 0 \\ 0 & \frac{1}{12}\cdot m_w \cdot 3(r^2_{w(out)} + r^2_{w(in)} + h^2_w) & 0 \\ 0 & 0 & \frac{1}{12}\cdot m_w \cdot 3(r^2_{w(out)} + r^2_{w(in)} + h^2_w) \end{bmatrix} \tag{4.5}$$

Let h^2_w denote the reaction wheel disk height.

Assuming Table 4.2 values, the RSA sphere and each RW (considering a RW arrangement composed of four RWs) have the following inertia tensors,

$$J_s = \begin{bmatrix} 0.0060 & 0 & 0 \\ 0 & 0.0060 & 0 \\ 0 & 0 & 0.0060 \end{bmatrix} [Kg\ m^2] \tag{4.6}$$

$$J_{wi} = \begin{bmatrix} 0.0024 & 0 & 0 \\ 0 & 0.0006 & 0 \\ 0 & 0 & 0.0006 \end{bmatrix} [Kg\ m^2] \tag{4.7}$$

Consequently, analysing both RTD inertia tensors (4.6) and (4.7), it is expected that the RSA requires less angular motion compared to a RW arrangement in order to produce the same amount of reaction torque.

The following simulations show both the RSA and RW arrangement performance for some desired satellite attitude maneuvers. Moreover two RW arrangements configurations are considered. Therefore the following three distinct RTDs are analysed:

- RSA with four active actuators in a tetrahedral geometry.
- RW arrangement with three reaction wheels in an orthogonal disposition
- RW arrangement with four reaction wheels in a tetrahedral geometry (L_2 optimization).

Figures 4.10, 4.11 and 4.12 denote a $\varphi = \frac{3\pi}{4}$ satellite attitude maneuvering for the referred three distinct RTDs. It's easily seen that for all cases the satellite converges to the desired attitude.

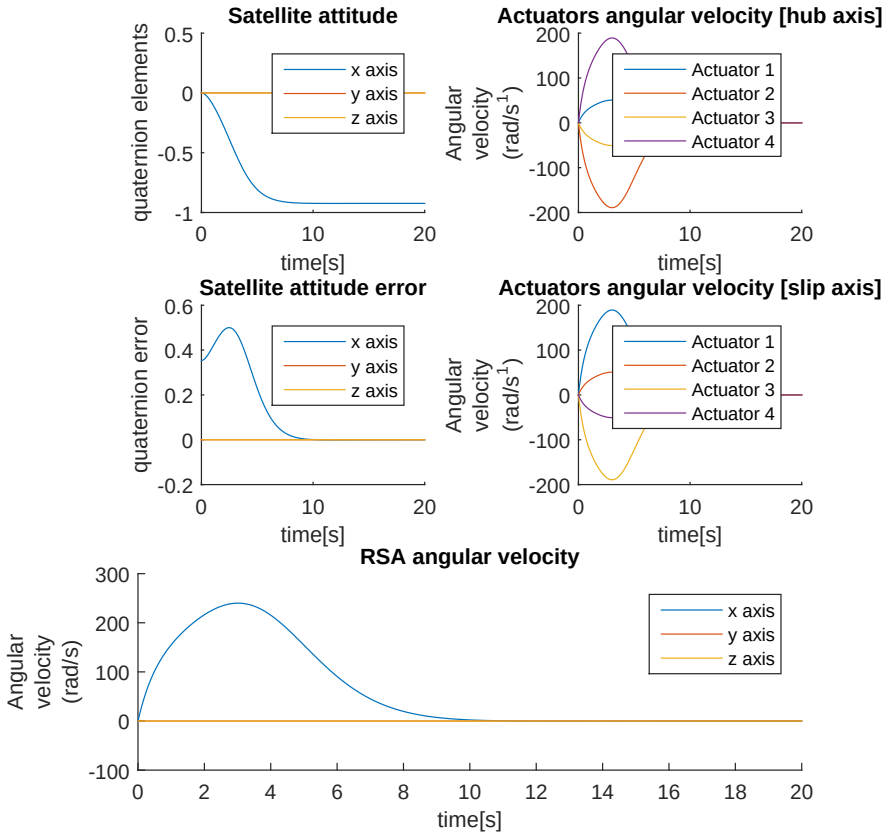

Figure 4.10: SACS with RSA, rotation of $\varphi = \frac{3\pi}{4}$

For simplicity it's assumed an unitary gear ratio between the RSA actuators radius and sphere radius. Note that both RW arrangement configurations (Figure 4.11 and 4.12) reach higher angular velocity values compared to RSA. These are a consequence of the RW inertia tensor, as it will be seen further ahead.

The RTDs mechanical work and attitude convergence times corresponding to Figures 4.10, 4.11 and 4.12, are denoted in Table 4.3.

Table 4.3: SACS simulation for RTD mechanical work comparison, $\varphi = \frac{3\pi}{4}$ rotation

RTD type	Mechanical work	Convergence time
RSA with four actuators (tetrahedral configuration)	348 $Joule$	10 s
Three RW arrangement (orthogonal configuration)	664.3 $Joule$	10 s
Four RW arrangement (tetrahedral configuration)	664.3 $Joule$	10 s

Applying equal controller gains for both RTDs simulations, the SACS ensures that each RTD produces the same reaction torque. For instance, for a $\varphi = \frac{3\pi}{4}$ satellite attitude maneuvering it can be seen that the produced reaction torques are equivalent for both RTDs, see Figure 4.13.

Therefore, since each RTD ensures the same torque production and requires distinct mechanical work values to achieve it, is clear that their performances in energy terms are not equal. Furthermore

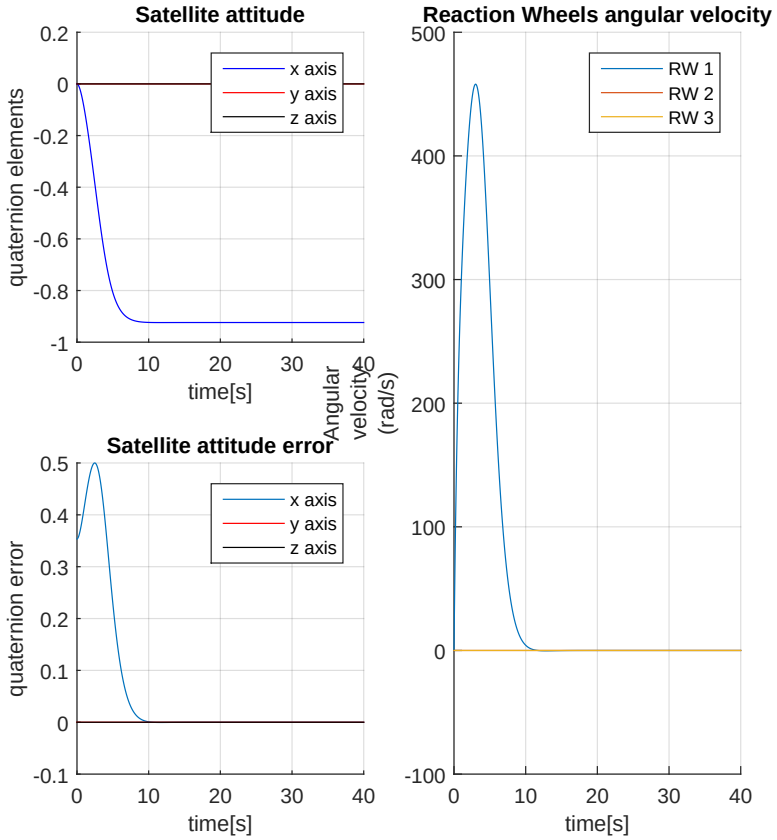

Figure 4.11: SACS with three RWs, rotation of $\varphi = \frac{3\pi}{4}$

Table 4.3 shows another important aspect regarding RW arrangements. Balanced[1] geometrical RW arrangements have the same mechanical work to perform a given satellite attitude maneuvering. Hence, RW arrangements with balanced geometries differ only in maximum torque capability and RW failure tolerance.

Table 4.4 shows both convergence time and mechanical work values expended by each RTD for additional satellite attitude maneuverings. Additionally since balanced RW arrangements spend the same energy, only a four RW according to a regular tetrahedral geometry is illustrated.

Inspecting the obtained results the RSA energy efficiency can be compared to RW arrangements. It becomes now clear that there's a constant relation between the RSA mechanical work and equivalent RW arrangement. The RSA mechanical work reduction compared to the RW arrangement comes strictly from its inertia tensor matrices. The SACS controller ensures that both RTDs apply the same reaction torque to the satellite, thus since their inertia tensors are distinct they require different angular accelerations resulting in distinct total angular displacements for the same convergence time. Hence the relation between the RSA and RW arrangement mechanical work is equivalent to,

$$K = \frac{W_{RW}}{W_{RSA}} = \frac{\sum J_{rw\ ii}}{\sum J_{s\ ii}} \tag{4.8}$$

[1] Balanced geometries correspond to have a fixed relation between all RWs rotation axis, see (B.10)

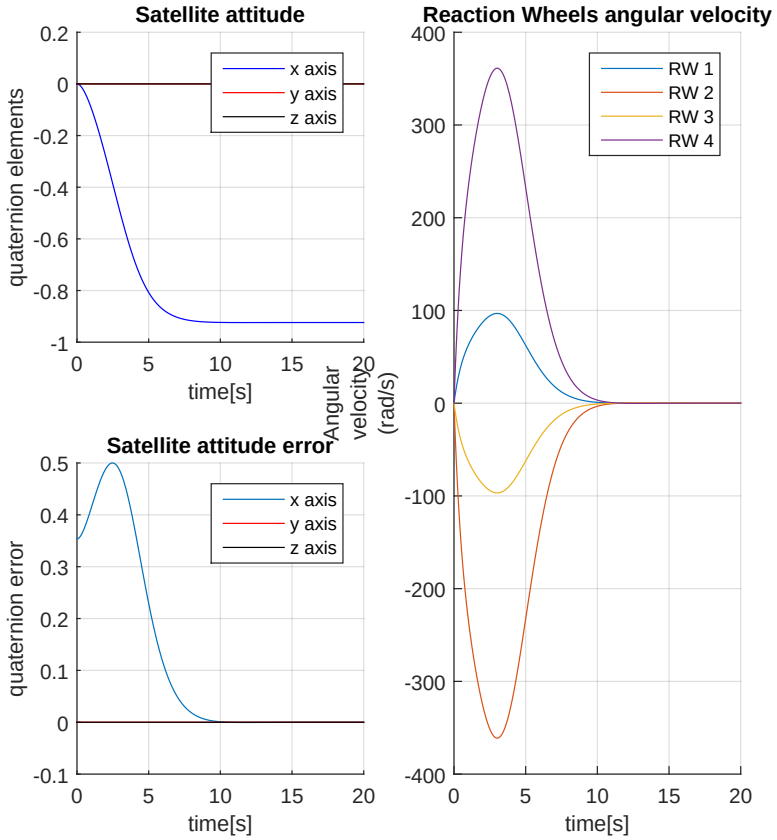

Figure 4.12: SACS with four RWs (L_2 optimization), rotation of $\varphi = \frac{3\pi}{4}$

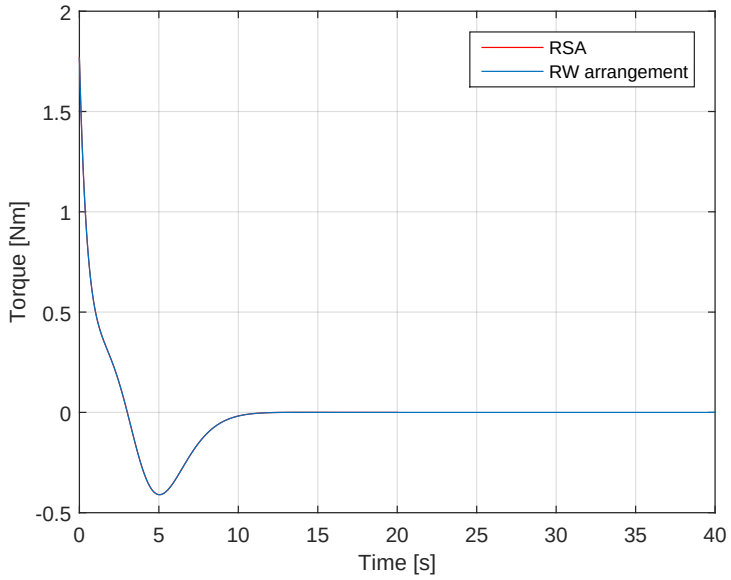

Figure 4.13: Reaction torque applied to the satellite for both RTDs for a $\varphi = \frac{3\pi}{4}$ rotation

where $J_{j\ ii}$ denote each j body principal moment of inertia. Note that this expression is only valid assuming that both RTD inertia tensors are diagonal. Considering Table 4.2 and assuming a RW arrangement

Table 4.4: Additional SACS simulations for RTD mechanical work comparison

RTD type	Mechanical work	Convergence time
$\phi = \frac{\pi}{2}$ rotation		
RSA	285 $Joule$	8.1 s
RW arrangement	544 $Joule$	8.1 s
$\varphi = \frac{\pi}{6}$, $\theta = \frac{\pi}{3}$ rotation		
RSA	198.7 $Joule$	7.4 s
RW arrangement	373.5 $Joule$	7.4 s
$\theta = \frac{\pi}{3}$, $\varphi = \frac{-2\pi}{7}$ rotation		
RSA	240.9 $Joule$	7.6 s
RW arrangement	459.8 $Joule$	7.6 s

composed of four RWs this value yields,

$$K = \frac{4 \times 0.0024}{3 \times 0.0060} \approx \frac{240.9}{459.8} \approx \frac{198.7}{373.5} \approx \frac{285}{544} \approx 0.53 \tag{4.9}$$

Note that the same result would be obtained if a RW arrangement composed by three RWs was considered. Therefore, the RSA with a hollow sphere spends approximately half the energy to produce the same torque generated from a RW arrangements.

Additionally for a RSA composed of a solid sphere it would be still more energy efficient compared to the same RW arrangement. The solid sphere inertia tensor is given by (4.10).

$$J_{s\ solid} = \begin{bmatrix} \frac{2}{5} \cdot m_s \cdot r_s^2 & 0 & 0 \\ 0 & \frac{2}{5} \cdot m_s \cdot r_s^2 & 0 \\ 0 & 0 & \frac{2}{5} \cdot m_s \cdot r_s^2 \end{bmatrix} \tag{4.10}$$

Hence for a solid sphere with $1\ Kg$ mass and $10\ cm$ radius, the energy gain compared to the previous RW arrangement is given by (4.11).

$$K = \frac{4 \times 0.0024}{3 \times 0.0040} = 0.8 \tag{4.11}$$

Therefore, even if the RSA sphere is solid which has lower moment of inertia compared to a hollow one it is still more energy efficient compared to a RW arrangement.

Hence, in general the RSA is more energy efficient compared to a RW arrangement, or equivalently it can be lighter compared to a RW arrangement, for the same reaction torque production.

4.3 RTDs physical construction constraints

The previous two Sections, 4.1 and 4.2 assumed an ideal environment, thus not considering uncertainties, losses or external forces affecting the satellite and RTDs models. Therefore, despite this study doesn't analyses such factors, they may have significant impact upon this thesis results.

Section 3.1 describes a generic satellite model which can consider external torques applied to the satellite (e.g. solar radiation pressure, gravity gradient, particle collision with the satellite and others). Furthermore, it is assumed that the satellite attitude is fully known, not corresponding to a real-world situation. Hence a satellite attitude estimation strategy must be defined and considered.

Concerning RTDs, there are also factors that affect their performance. Regarding the RSA, it is assumed that there are mainly four factors that could have a negative impact upon its performance, namely:

- Rolling mechanical contact slippage between the actuators and the sphere surface
- Non-uniform spherical mass (i.e. a non-diagonal sphere inertia tensor)
- Actuation system DC motor motion de-synchronization
- DC Motor disturbances

The RSA sphere and actuators materials may probably have a considerable impact upon the RSA performance. Thus, the materials should be chosen in order to minimize the actuators slippage behaviour. Furthermore, since it does not exist a real prototype of a RSA, there's not any information about how each constraint affects its real performance.

Regarding RW arrangements, there are mainly two issues, namely:

- RW disk mass unbalance (i.e. a non-diagonal RW inertia tensor)
- DC motor disturbances

These two factors may have a negative impact upon the RW arrangement performance. Note that, although there are similarities between both RTDs physical construction constraints, they may have different impacts on both RTDs performances. Thus a real-word comparison of both RTDs should be considered to verify this thesis theoretical results.

Chapter 5

Conclusions

This thesis conducted a study regarding a new reaction torque device concept, the RSA. This study covers the device feasibility proof and its benefits compared other RTDs. The referred feasibility study considers three stages, proving different RSA features and allowing distinct conclusions.

The first stage concerns the RSA motion capability, i.e prove that it is feasible in kinematic terms (see Chapter 2). The rolling contact kinematics concepts were particularly useful to describe mechanical rolling contact between the actuator system and the sphere surface. In fact, these concepts could be applied to describe spheroids besides the spherical one, and study their kinematic model.

The RSA kinematic analysis division in two steps, namely the rolling sphere on a plane and mobile holonomic robot, simplified the RSA overall study. If such approach was not considered, it would be required to compute the holonomic wheel surface geometric parameters which would demand several mappings leading to a more complex model.

Given that both the rolling sphere and mobile robot move on a plane surface and are both controllable, their combination, i.e. the actuator system in mechanical contact with the sphere surface can induce any angular motion to the RSA sphere. This result proves the RSA feasibility in kinematic terms partially supporting the intuition that motivated this device study.

Chapter 3 illustrates a RSA example concerning an actuation system according to a regular tetrahedral geometry. Note that several different actuator system geometries could have been analysed, however only the regular tetrahedral geometry was considered for this thesis. The tetrahedral configuration showed to be a RSA suitable configuration, being an balanced arrangement and ensuring the RSA sphere static equilibrium (stage two). Furthermore, the static equilibrium proved a RSA important feature, the sphere geometrical center remained fixed with respect to a given inertial frame in the RSA outer shell, allowing sphere pure rotation motions.

The RSA *Jacobian* describes the actuators motion with respect to the sphere motion. The *Jacobian* analysis showed the RSA singularity-free feature (stage three) and the actuators unique combined motion for a given sphere angular motion. With such analysis the RSA could be fully described concerning its composing bodies motion when a given reaction torque was demanded. Consequently these three stages prove the RSA device feasibility.

The RSA performance comparison to other RTDs, such as RW arrangements considered a simulation environment capable of testing each RTD. Furthermore a SACS Simulink® model considering a RTD device, provided a better grasp of the satellite behaviour concerning RTDs operation. Such model aimed to represent a simple yet complete SACS simulator which could be constantly improved by the inclusion of additional effects. Nevertheless, this study considers only the satellite and RTD general dynamics since it is intended to perform a general RTD comparison neglecting losses and disturbances.

The RTDs performance metric choice considers an energy consumption in terms of mechanical work. Other alternatives could have been considered, although they would be consequences of this main result and probably require the definition of other physical parameters, such as motor specifications, friction between surfaces and others. Hence the energy analysis confirmed the advantages of a RSA device compared to RW arrangements when both RTDs were implemented in the same SACS model. The results obtained in Chapter 4 showing the RSA energy consumption to be approximately half compared to one spent by RW arrangements prove the intuition regarding the RSA benefits.

5.1 Future Work

The present thesis considers a RSA device introductory analysis. Therefore, there's a vast number of studies that could be performed in future work. For simplicity consider the following list containing some future work topics:

- Analyse and model the Holonomic wheels slip behaviour.
- Compare distinct holonomic wheels types performance.
- Describe the friction contact force between the actuators and sphere surface for different reaction torques generation intervals.
- Consider a set of specific DC motors and their control law. Analyse the required motor synchronization and what effects it could have in the RSA performance if such synchronism was not achieved.
- Compare different actuator systems geometries and their consequences for motor load sharing and actuator failure tolerance.
- Define a strategy for the sphere motion observability.
- Study the advantages and disadvantages of considering a non-spherical body for reaction torque production.
- Study the feasibility of a support/suspension system coupling the actuation system to the RSA outer shell and what benefits could it have in reducing motor de-synchronization as well in adapting to other rotating bodies geometries, see Figure 5.1.
- Build a RSA prototype and measure its real performance verifying if the same energy efficiency is valid in a real world situation.

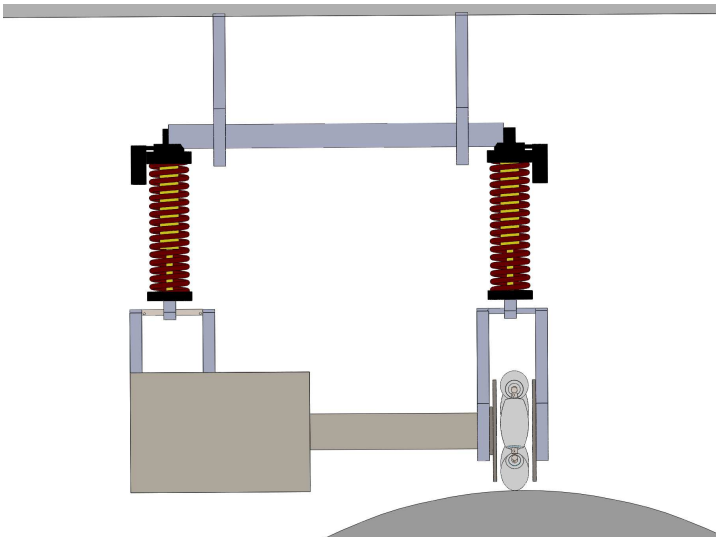

Figure 5.1: RSA actuating system with support/suspension system

The referred topics consist in some problems that could be analysed to continue this RSA study.

Bibliography

[1] V.I Arnold. *Mathematical Methods of Classical Mechanics*. Springer-Verlag, 2^{nd} edition, 1991. ISBN:0-387-96890-3.

[2] J. C. A. Barata and M. S. Hussein. The Moore-Penrose Pseudoinverse. A Tutorial Review of the Theory. Technical report, Instituto de Física, Universidade de Sao Paulo, October 2011.

[3] Guy Campion, Georges Bastin, and Brigitte D'Andrea-Novel. Structural Properties and Classification of Kinematic and Dynamic Models of Wheeled Mobile Robots. *IEEE Transaction on Robotics and Automation*, 12(1), February 1996.

[4] Mogens Blanke and Martin Birkelund Larsen. Satellite Dynamics and Control in a Quaternion Formulation. Technical report, DTU Electrical Engineering Department, 2010.

[5] Manfredo P. Do Carmo. *Differential Geometry of Curves and Surfaces*. Pearson, 1^{st} edition, 1976. ISBN:978-0132125895.

[6] Howard D. Curtis. *Orbital Mechanics for Engineering Students*. Butterworth Heinemann, 2^{nd} edition, 2010. ISBN: 978-0123747785.

[7] Valdemir Carrara , Adolfo Graciano da Silva and Hélio Koiti Kuga. A Dynamic Friction Model for Reaction Wheels. *IAA*, 2012.

[8] Ferdinand P. Beer , E. Russell Johnston Jr. , David F. Mazurek , Phillip J. Cornwell , Elliot R . Eisenberg. *Vector Mechanics for Engineers: Statics and Dynamics*. McGraw-Hill, ninth edition edition, 2010.

[9] Peter Fankhauser and Corsin Gwerder. Modeling and Control of a Ballbot. Master's thesis, ETH Zurich, Spring Term 2010.

[10] Andrew J. Hanson. *Vizualing Quaternions*. Elsevier, 1^{st} edition, 2006. ISBN: 978-0-12-088400-1.

[11] Giovanni Indiveri. Swedish Wheeled Omnidirectional Mobile Robots: Kinematics Analysis and Control. *Transactions on Robotics*, 25(1), February 2009.

[12] Zuliana Ismail and Renuganth Varatharajoo. A Study of Reaction Wheel Configurations for a 3-axis Satellite Attitude Control. *Advances in Space Research*, 2009.

[13] Dong-Ik Cheon, Eun-Jeong Jang, and Hwa-Suk Oh. Reaction Wheel Disturbance Reduction Method Using Disturbance Measurement Table. *Journal of Astronomy and Space Sciences*, 2011.

[14] Jorge V. José and Eugene J Saletan. *Classical Dynamics: A Contemprary Approach*. Cambridge University Press, 1^{st} edition, 1998. ISBN:0-521-63176-9.

[15] S. Widnall J.Peraire. 3D Rigid Body Dynamics: The Inertia Tensor. Technical report, MIT, Fall 2008.

[16] Marcel J.Sidi. *Spacecraft Dynamics and Control*. Cambridge University Press, 1^{st} edition, 1997. ISBN: 0-521-55072-6.

[17] T. B. Lauwers, G. A. Kantor, and R. L. Hollis. A Dynamically Stable Single-Wheeled Mobile Robot with Inverse Mouse-Ball Drive. *IEEE International Conference on Robotics and Automation*, May 2006. Orlando, FL.

[18] Ibrahim Kök. Comparison and Analysis of Attitude Control Systems of a Satellite Using Reaction Wheel Actuators. Master's thesis, University of Würzburg, October 2012.

[19] A. Weiss, R. Langlois and M. J. D. Hayes. Unified Treatment of the Kinematic Interface Between a Sphere and Omnidirection Wheel Actuators. *Journal of Mechanisms and Robotics*, 3, November 2011.

[20] M. John D. Hayes , Robert Langlois and Abraham Weiss. Atlas motion platform generalized kinematic model. *Springer*, November 2010.

[21] Alan F. Ma and Nikola N. Dominikovic. Three-Axis Stabilized Earth Orbiting Spacecraft Simulator. Master's thesis, California Polytechnic State University, Octobor 2012. Aerospace Engineering Department.

[22] F. Landis Markley and John L. Crassidis. *Fundamentals of Spacecraft Attitude Determination and Control*. Springer, 1^{st} edition, 2014. ISBN: 978-1-4939-0801-1.

[23] Landis Markley and R. G. Reynolds. Maximum Torque and Momentum Envelopes for Reaction Wheel Arrays. *Journal of Guidance Control and Dynamics*, July 2001.

[24] David J. Montana. The Kinematics of Contact and Grasp. *The International Journal of Robotics*, 7(3), June 1988. Massachussetts Institute of Technology.

[25] Oludayo John Oguntoyinbo. PID Control of Brushless DC Motor and Robot Trajectory Planning Simulation with MATLAB/SIMULINK. Master's thesis, Vaasan Ammattikorkeakkoulu University of Applied Sciences, December 2009.

[26] Richard M. Murray, Zexiang Li, S. Shankar Sastry. *A Mathematical Introduction to Robotic Manipulation*. CRC Press, 1^{st} edition, 1994. ISBN: 978-0849379819.

[27] Ryan E. Snider. Attitude Control of a Satellite Simulator Using Reaction Wheels and a PID Controller. Master's thesis, Air Force Institute of Technology , Ohio, March 2010. Department of Aeronautics and Astronautics.

[28] H. J. Sussmann. A General Theorem on Local Controllability. *Control and Optimization*, 25(1), January 1987.

[29] Mikhail Svinin and Shigeyuki Hosoe. On the Dynamics and Motion Planning for a Rolling System With Variable Inertia. *International Conference on Intelligent Robots and Systems*, October 2007. San Diego, CA, USA.

[30] Bruno Siciliano, Lorenzo Sciavicco , Luigi Villani and Giuseppe Oriolo. *Robotics: Modelling, Planning and Control*. Springer, 2009. ISBN 978-1-84628-641-4.

[31] Ronny Votel and Doug Sinclair. Comparison of Control Moment Gyros and Reaction Wheels for Small Earth-Observing Satellites. *AIAA/USU*. Conference on Small Satellites.

Appendix A

Rotational mechanics fundamentals

A.1 Theoretical Concepts of Classical Mechanics

This Appendix shows some classical mechanics concepts, consisting of the required theoretical background for RTD dynamics understanding.

Some principles and concepts presented in this Appendix are analysed in more detail in [1] and [14].

A.1.1 Newtonian Mechanics

Newtonian Mechanics allow the motion study of point masses systems in a three-dimensional Euclidean space $\mathbb{R}^3$. Furthermore, it characterizes forces both in translational and rotational motion.

For satellite attitude motion analysis purposes, translational movements can be neglected since the satellite and therefore the RTD are in torque-free situation, where only rotational movements are of concern. Newtonian Mechanics relies upon three main laws describing essentially the dynamics of body non-relativistic motions. The proof of such laws is not considered here, but only their final result, for further details see [1] and [14].

Consider respectively the first second and third Newton laws.

- If no external forces are applied to a given body, it either remains at rest or continues to move at a constant velocity when it is observed from an inertial reference frame.
- The force acting on a given particle or body is defined by

$$F = ma = \frac{d^2x}{dt^2} \tag{A.1}$$

- Consider the interaction between two particles 1 and 2. For a force $F_{12} = m_1 a_1$ on particle 1 due to the presence of particle 2 (or by particle 2). Similarly, there is a force $F_{21} = m_2 a_2$ on particle 2 by particle 1. Which corresponds to writing that,

$$F_{12} + F_{21} = 0 \tag{A.2}$$

It is also important to describe a system according to a energy analysis, hence assuming a constant system energy (conservation of energy principle), one can write that,

$$E = T + U \tag{A.3}$$

where E denotes the system total energy and T and U denote respectively the kinetic and potential energy.

The RTD dynamics study demands the understanding of angular momentum concept and its conservation law. Usually one is acquainted with the notion of linear momentum p for a given particle of mass m moving at velocity v according to a translation trajectory.

$$p = mv \tag{A.4}$$

According to conservation of energy principle, a system composed of two isolated particles has its particle linear momenta sum constant. Analogously there's also an angular momentum conservation for rotational motions. The angular momentum h of a particle about some point S is defined in terms of its (linear) momentum p as follows,

$$h = x \times p \tag{A.5}$$

Where x is the object position measured from the point S. Equivalently, (A.5) yields,

$$h = m\omega \tag{A.6}$$

where ω denotes the particle angular velocity defined as $\omega = x \times v$.

Considering (A.5) time derivative, it yields,

$$\dot{h} = \dot{x} \times p + x \times \dot{p} = v \times p + x \times ma \tag{A.7}$$

The first cross product in (A.7) can be written as,

$$v \times p = v \times mv = m(v \times v) = 0 \tag{A.8}$$

thus,

$$\dot{h} = x \times F = \tau \tag{A.9}$$

where τ denotes a torque about point S. (A.9) shows a very important aspect regarding RTDs basic principle operation. Thus, due to angular momentum conservation, if a particle angular momentum changes so the remaining particle angular momentum change in opposite direction.

A.1.2 Rigid Bodies

Let q be a Cartesian vector relative to an inertial coordinate system k (which is assumed to be stationary), and Q a Cartesian vector of the same point relative to a *moving* coordinate system K.

Definition: Let k and K be oriented Euclidean spaces. A motion of K relative to k is a mapping smoothly depending on t:

$$D_t : K \to k \tag{A.10}$$

which preserves the metric and orientation. This motion D_t can be decomposed as the product of a rotation B_t and translation C_t as seen in Figure A.1.

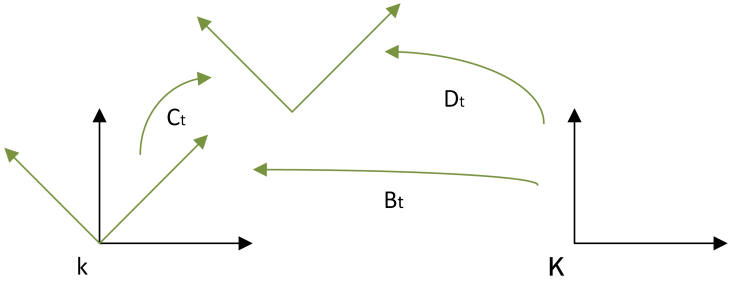

Figure A.1: Decomposition of motion D_t

Moreover, let k be a stationary coordinate system and K be a moving one, where $q(t) \in K$ is a moving point vector relative to the stationary system k, defined as,

$$q(t) = D_t Q(t) = B_t Q(t) + r(t) \tag{A.11}$$

and $Q(t)$ denotes the point vector relative to the moving system K. *Figure* A.2 illustrates these frames as well as the transformations between them.

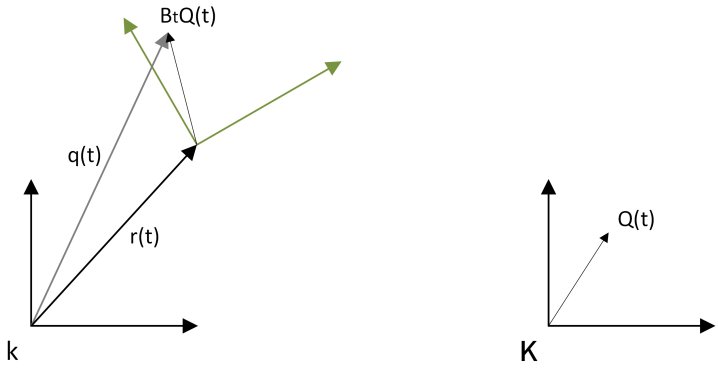

Figure A.2: Transformations between frames

Hence the ”absolute velocity” in terms of the relative motion $Q(t)$ can be computed by differentiating (A.11) with respect to t the velocities expression, yielding,

$$\dot{q} = \dot{B}Q + B\dot{Q} + \dot{r} \tag{A.12}$$

The meaning of these three terms can be clarified considering for instance a translational motion ($\dot{B} = 0$). Hence (A.12) is equivalent to $\dot{q} = B\dot{Q} + \dot{r}$.

Theorem If a moving system K has translational motion relative to k, then the absolute velocity is equivalent to the sum of the relative velocity and K system motion velocity, as follows,

$$v = v_{rel} + v_o \tag{A.13}$$

where,

- $v = \dot{q} \in k$ is the absolute velocity
- $v_{rel} = B\dot{Q} \in k$ is the relative velocity (distinct from $\dot{Q} \in K$)
- $v_o = \dot{r} \in k$ is the velocity of motion of the moving coordinate system.

Angular velocity

Consider a point at rest in K (*i.e.* $\dot{Q} = 0$) and a coordinate system K with only rotational motion (i.e. , $R = 0$). For this case the motion of $q(t)$ is called a *transferred rotation*.

Theorem At every time instant t, there is a vector $\omega(t) \in k$ such that the transferred velocity can be expressed as,

$$\dot{q} = \omega \times q \tag{A.14}$$

where ω denotes the instantaneous angular velocity; clearly it is uniquely defined by (A.14), see Figure A.3 for its illustration.

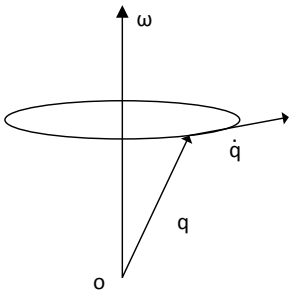

Figure A.3: Angular Velocity

Corollary. Consider a rigid body K with rotational motion around a stationary point o of space k. Hence, at every time instant, there exists an instantaneous rotation axis with respect to the referred motion.

The instantaneous axis of rotation in k is given by vector Ω, whereas for K the corresponding vector is denoted as $\omega = B^{-1}\Omega \in K$, where ω is the vector of angular velocity in the body. Therefore according to (A.12) it yields that $\dot{q} = \dot{B}Q$. Moreover writing Q in terms of q, gives,

$$\dot{q} = \dot{B}B^{-1}q = Aq \tag{A.15}$$

where $A = \dot{B}B^{-1} : k \to k$ is a linear operator on k.

Knowing that A is skew-symmetric, see [1], one can write (A.14) as,

$$\dot{q} = S(\omega)q = \omega \times q \tag{A.16}$$

Note that in Cartesian coordinates the operator $S(\omega)$ is given by an antisymmetric matrix (A.17).

$$S(\omega) = \begin{bmatrix} 0 & -\omega_z & \omega_y \\ \omega_z & 0 & -\omega_x \\ -\omega_y & \omega_x & 0 \end{bmatrix} \tag{A.17}$$

Thus matrix $S(\omega)$ can be seen as an angular velocity cross product equivalence. Suppose now that system K rotates ($r = 0$), and that a point in K is moving ($\dot{Q} \neq 0$). From (A.12) yields,

$$\dot{q} = \dot{B}Q + B\dot{Q} = [\omega \times q] + v_{rel} \tag{A.18}$$

Theorem: If a moving system K rotates relative to $o \in k$, then the absolute velocity is equal to the sum of the relative velocity and transferred velocity:

$$v = v_{rel} + v_n \tag{A.19}$$

where

- $v = \dot{q} \in k$, is the absolute velocity
- $v_{rel} = B\dot{Q} \in k$, is the relative velocity
- $v_n = \dot{B}Q = [\omega \times q] \in k$, is the transferred velocity of rotation

Consider now rotating frames. Let $B_t : K \to k$ be a frame K rotation relative to frame k, which is stationary. Moreover, let $Q(t) \in K$ be a moving point vector in the moving frame, $q(t) = B_t Q(t) \in k$ be a moving point vector in the stationary frame and Ω be the angular velocity vector in the moving frame.

According to Newton's second law, the motion of q in k can be described as,

$$m\ddot{q} = f(q, \dot{q}) \tag{A.20}$$

Theorem: There are three types of inertial forces acting upon every moving point Q of mass m, in a rotating coordinate system.

- The inertial force of rotation: $m(\dot{\omega} \times Q)$
- The Coriolis force: $2m(\omega \times \dot{Q})$
- The centrifugal force: $m(\omega \times (\omega \times Q))$

The inertial force of rotation occurs only when angular velocity variations occur, and describes reaction torques for a body angular momentum variation. The two remaining forces are present even in uniform rotation, see Figure A.4.

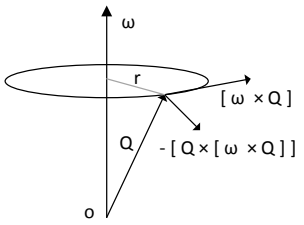

Figure A.4: Forces in constant rotational motion

Unlike translational rigid bodies motion a rotational motion requires a full body mass distribution characterization. Therefore, it is required to define the body mass distribution according to an inertia tensor, defined as,

$$J = \begin{bmatrix} J_{xx} & -J_{xy} & -J_{xz} \\ -J_{yx} & J_{yy} & -J_{yz} \\ -J_{zx} & -J_{zy} & J_{zz} \end{bmatrix} \tag{A.21}$$

Substituting (A.21) in (A.6) yields,

$$\begin{bmatrix} h_x \\ h_y \\ h_z \end{bmatrix} = \begin{bmatrix} J_{xx} & -J_{xy} & -J_{xz} \\ -J_{yx} & J_{yy} & -J_{yz} \\ -J_{zx} & -J_{zy} & J_{zz} \end{bmatrix} \begin{bmatrix} \omega_x \\ \omega_y \\ \omega_z \end{bmatrix} \tag{A.22}$$

For further details regarding the inertia tensor computation for a given rigid body see [15].

A.1.3 Euler's equations

Euler's equations describe rotational body motion dynamics, thus they are essential to fully understand satellites dynamic behaviour with coupled RTDs. This Appendix Subsection describes Euler's equations for a general case, these concepts can be found in more detail in [6].

Rigid body rotational motions around its center of mass G or around a fixed point P verify (A.9) which states that,

$$\tau = \dot{h} \tag{A.23}$$

, where τ denotes the rigid body torque.

Considering a co-moving coordinate frame xyz (composed by unitary components $\vec{e_x}$,$\vec{e_y}$ and $\vec{e_z}$), with angular velocity Ω with respect to point G or P. The angular momentum can be decomposed in three components of space.

$$h = h_x\vec{e_x} + h_y\vec{e_y} + h_z\vec{e_z} \tag{A.24}$$

For simplicity consider that,

1. The moving xyz axes are the principal axes of inertia, and

2. The moments of inertia relative to xyz are constant in time.

According to (A.22), and considering a rigid body with all three planes xy,yz and xz being planes of symmetry with respect to the mass distribution, (A.24) can be written as,

$$h = J_{xx}.\Omega_x\vec{e_x} + J_{yy}.\Omega_y\vec{e_y} + J_{zz}.\Omega_z\vec{e_z} \tag{A.25}$$

The theorem of transferred velocity of a rigid body motion between frames, given by (A.19), allows to write angular momentum for such rigid body as,

$$\tau = \dot{h}_{rel} + \Omega \times h \tag{A.26}$$

note that, Ω refers to the moving xyz coordinate system angular velocity and ω refers to body angular velocity, both described with respect to xyz non-inertial frame components.

$$\omega = \omega_x\vec{e_x} + \omega_y\vec{e_y} + \omega_z\vec{e_z}$$

$$\Omega = \Omega_x\vec{e_x} + \Omega_y\vec{e_y} + \Omega_z\vec{e_z}$$

The absolute angular acceleration can be also devised according to the theorem of transferred velocity (A.19). Thus, it becomes,

$$\alpha = \dot{\omega} = \frac{d\omega_x}{dt}\vec{e_x} + \frac{d\omega_y}{dt}\vec{e_y} + \frac{d\omega_z}{dt}\vec{e_z} + \Omega \times \omega \tag{A.27}$$

Solving the cross product in (A.27), the angular acceleration becomes,

$$\alpha = \underbrace{(\dot{\omega_x} + \Omega_y\omega_z - \Omega_z\omega_y)\vec{e_x}}_{\alpha_x} + \underbrace{(\dot{\omega_y} + \Omega_z\omega_x - \Omega_x\omega_x)\vec{e_y}}_{\alpha_y} + \underbrace{(\dot{\omega_z} + \Omega_x\omega_y - \Omega_y\omega_x)\vec{e_z}}_{\alpha_z} \tag{A.28}$$

Hence, it is usually true that,

$$\alpha_x \neq \dot{\omega}_x \;\; \alpha_y \neq \dot{\omega}_y \;\; \alpha_z \neq \dot{\omega}_z \tag{A.29}$$

Considering the transferred velocity theorem (A.19), the rigid body relative angular momentum derivative in (A.26) becomes,

$$\dot{h}_{rel} = \frac{d(J_{xx}\omega_x)}{dt}\vec{e_x} + \frac{d(J_{yy}\omega_y)}{dt}\vec{e_y} + \frac{d(J_{zz}\omega_z)}{dt}\vec{e_z} \tag{A.30}$$

Assuming J_{xx},J_{yy} and J_{zz} to be constant values, (A.30) yields,

$$\dot{h}_{rel} = J_{xx}.\dot{\omega}_x\ \vec{e_x} + J_{yy}.\dot{\omega}_y\ \vec{e_y} + J_{zz}.\dot{\omega}_z\ \vec{e_z} \tag{A.31}$$

Combining (A.26) and (A.31) follows,

$$\tau = J_{xx}.\dot{\omega}_x\ \vec{e_x} + J_{yy}.\dot{\omega}_y\ \vec{e_y} + J_{zz}.\dot{\omega}_z\ \vec{e_z} + \begin{vmatrix} \vec{e_x} & \vec{e_y} & \vec{e_z} \\ \Omega_x & \Omega_y & \Omega_z \\ \omega_x & \omega_y & \omega_z \end{vmatrix} \tag{A.32}$$

Moreover expanding (A.32) in three-dimensions and computing the cross product yields,

$$\begin{aligned} \tau_x &= J_{xx}.\dot{\omega}_x + J_{zz}\ .\ \Omega_y\ .\ \omega_z - J_{yy}\ .\ \Omega_z\ .\ \omega_y \\ \tau_y &= J_{yy}.\dot{\omega}_y + J_{xx}\ .\ \Omega_z\ .\ \omega_x - J_{zz}\ .\ \Omega_x\ .\ \omega_z \\ \tau_z &= J_{zz}.\dot{\omega}_z + J_{yy}\ .\ \Omega_x\ .\ \omega_y - J_{xx}\ .\ \Omega_y\ .\ \omega_x \end{aligned} \tag{A.33}$$

If the co-moving frame xyz is rigidly attached to the body frame, then its angular velocity is the same as that of the body, i.e. , $\Omega = \omega$. For such case (A.33) reduces to the classical Euler equations, as follows,

$$\tau = \dot{h}_{rel} + \omega \times h \tag{A.34}$$

Expanding (A.34) with respect to the three components, $\vec{e_x}$, $\vec{e_y}$ and $\vec{e_z}$ yields,

$$\begin{aligned} \tau_x &= J_{xx}.\dot{\omega}_x + (J_{zz} - J_{yy})\omega_y\omega_z \\ \tau_y &= J_{yy}.\dot{\omega}_y + (J_{xx} - J_{zz})\omega_z\omega_x \\ \tau_z &= J_{zz}.\dot{\omega}_z + (J_{yy} - J_{xx})\omega_x\omega_y \end{aligned} \tag{A.35}$$

Appendix B

RSA Tetrahedral geometry

This appendix covers the actuator system study for a regular tetrahedral geometry configuration.

According to Section 2.3, some actuator systems composed of at least three holonomic actuators are capable of moving without constraints on a surface, thus being controllable. Therefore, actuator systems composed of three or more actuators, may confer three independent rotational DOF to the RSA sphere. Hence it is possible to create reaction torques according to any direction.

The regular tetrahedral geometry is considered due to its equilateral triangle facets composition, which according to Section 2.3 have performance benefits for systems composed of three holonomic actuators. Furthermore, a regular tetrahedral geometry proves to be an efficient way to dispose the actuators in a three-dimensional space.

Section B.1 analyses the sphere static equilibrium issue, proving the referred regular tetrahedral geometry capability to guarantee the sphere static equilibrium.

Section B.2 shows a possible actuator rotational axes computation considering the constraints imposed by a regular tetrahedral geometry.

B.1 Static Equilibrium

The actuator system regular tetrahedral geometry, concerns four actuators contact points in contact with the sphere surface coincident with regular tetrahedron vertices circumscribed on the sphere, see Figure B.1. It is intended to analyse if the actuator system adopted geometry verifies the sphere static equilibrium. Furthermore the static equilibrium aims to prove the forces sum and moments sum acting on the sphere are zero. Consequently, the contact forces induced by the actuator system on the spherical

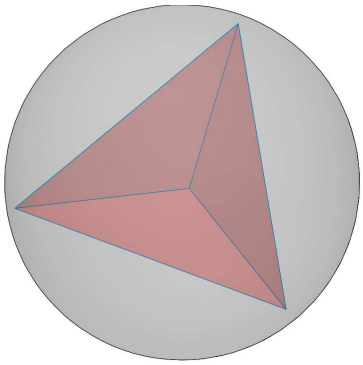

Figure B.1: Regular Tetrahedral Geometry

body surface have to verify (B.1).

$$\begin{cases} \sum F_x = 0 \\ \sum F_y = 0 \\ \sum F_z = 0 \\ \sum \tau_x = 0 \\ \sum \tau_y = 0 \\ \sum \tau_z = 0 \end{cases} \tag{B.1}$$

where F_i denotes the force along the i component of space, and τ_i denotes the force moment along the i component of space.

One intuitive solution for the given geometry is to consider the actuators to be perpendicular to the sphere surface, having its contact force vectors pointing from the tetrahedron vertices to the sphere center. Additionally, these force vectors are chosen to be coherent with the normal vectors defined by tetrahedron planes, see Figure B.2. For simplicity let us assume a unitary sphere mass.

Using MATLAB® symbolic language, one can compute the under-determined system solutions that relate the chosen four force vectors with (B.1). The referred four vectors are composed of three components each, given a total of twelve unknowns, see (B.2).

$$\begin{bmatrix} F_1 \\ F_2 \\ F_3 \\ F_4 \end{bmatrix} = \begin{bmatrix} a\vec{e_x} & b\vec{e_y} & c\vec{e_z} \\ d\vec{e_x} & e\vec{e_y} & f\vec{e_z} \\ g\vec{e_x} & h\vec{e_y} & i\vec{e_z} \\ j\vec{e_x} & k\vec{e_y} & l\vec{e_z} \end{bmatrix} \tag{B.2}$$

Considering that all vectors are described with respect to the sphere center reference frame, one can compute (B.1) solution for a given contact points and force vectors choice. Note that the momentum is defined as,

$$\tau = F \times \rho \tag{B.3}$$

where F denotes the force vector applied to a given point of space and ρ denotes the position vector of

the referred point with respect to the reference frame origin. Therefore (B.3) becomes,

$$\begin{bmatrix} \tau_x \\ \tau_y \\ \tau_z \end{bmatrix} = \begin{bmatrix} F_y\rho_z - F_z\rho_y \\ -F_x\rho_z + F_z\rho_x \\ F_x\rho_y - F_y\rho_x \end{bmatrix} \tag{B.4}$$

Expanding (B.1) with respect to four force vectors yields,

$$\begin{bmatrix} \sum F_x = 0 \\ \sum F_y = 0 \\ \sum F_z = 0 \\ \sum \tau_x = 0 \\ \sum \tau_y = 0 \\ \sum \tau_z = 0 \end{bmatrix} \equiv \begin{bmatrix} (a+d+g+j)\vec{e_x} = 0 \\ (b+e+h+k)\vec{e_y} = 0 \\ (c+f+k+l)\vec{e_z} = 0 \\ (b\rho_{1z} - c\rho_{1y} + e\rho_{2z} - f\rho_{2y} + h\rho_{3z} - k\rho_{3y} + j\rho_{4z} - l\rho_{4y})\vec{e_x} = 0 \\ (-a\rho_{1z} + c\rho_{1x} - d\rho_{2z} + f\rho_{2x} - g\rho_{3z} + k\rho_{3x} - j\rho_{4z} + l\rho_{4x})\vec{e_y} = 0 \\ (a\rho_{1y} - b\rho_{1x} + d\rho_{2y} - e\rho_{2x} + g\rho_{3y} - h\rho_{3x} + j\rho_{4y} - k\rho_{4x})\vec{e_z} = 0 \end{bmatrix} \tag{B.5}$$

Hence, as referred, the system is in fact under-determined, having twelve vector component unknowns for only six equations. Considering the reference frame and regular tetrahedral geometry origin to be coherent and defined at $[0, 0, 0]$, an example of a regular tetrahedron vertices can be defined as,

$$\begin{bmatrix} \rho_1 \\ \rho_2 \\ \rho_3 \\ \rho_4 \end{bmatrix} = \begin{bmatrix} -0.5775\vec{e_x} & 0.5775\vec{e_y} & 0.5575\vec{e_z} \\ -0.5775\vec{e_x} & -0.5775\vec{e_y} & -0.5575\vec{e_z} \\ 0.5775\vec{e_x} & -0.5775\vec{e_y} & 0.5575\vec{e_z} \\ 0.5775\vec{e_x} & 0.5775\vec{e_y} & -0.5575\vec{e_z} \end{bmatrix} \tag{B.6}$$

Considering the force vectors corresponding to the ρ_i vectors in (B.6), it is desired to show that the system is in fact in static equilibrium.

$$\begin{bmatrix} F_1 \\ F_2 \\ F_3 \\ F_4 \end{bmatrix} = \begin{bmatrix} 0.5775\vec{e_x} & -0.5775\vec{e_y} & -0.5775\vec{e_z} \\ 0.5775\vec{e_x} & 0.5775\vec{e_y} & 0.5775\vec{e_z} \\ -0.5775\vec{e_x} & 0.5775\vec{e_y} & -0.5775\vec{e_z} \\ -0.5775\vec{e_x} & -0.5775\vec{e_y} & 0.5775\vec{e_z} \end{bmatrix} \tag{B.7}$$

Using vectors (B.6) and force vector coordinates (B.7) it can be verified that this actuator geometric disposition choice achieves a static equilibrium, according to (B.5). *Figure* B.3 shows the vertices (contact points) and corresponding force vectors of this regular tetrahedral solution.

B.2 Actuators rotation axes determination

Section B.1 verifies the RSA sphere static equilibrium for an actuator system according to a regular tetrahedral geometry.

Based on the referred contact force vectors F_1, F_2, F_3, F_4, it is required to determine the actuators rotational axis vectors. The computation of these vectors can be also performed using MATLAB® sym-

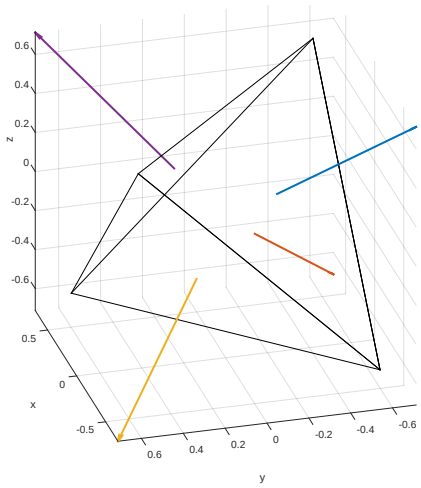

Figure B.2: Regular Tetrahedral Geometry with Facets Normal Vectors

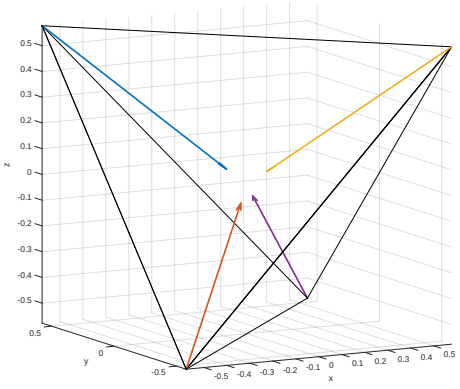

Figure B.3: Regular Tetrahedral Geometry Vertices and Force Vectors

bolic notation. The rotation axis vectors must be computed in order to achieve a balanced geometry that distributes as equally as possible the effort performed by all the actuators for a given spherical angular motion. To find such vectors consider the definition of two requirements as follows.

The first requirement concerns that any actuator i rotation axis must belong to the normal plane defined by actuator i contact force vector at intersection with the sphere surface. Such requirement can be written in mathematical terms as follows,

$$\begin{cases} \omega_1 F_1 = 0 \\ \omega_2 F_2 = 0 \\ \omega_3 F_3 = 0 \\ \omega_4 F_4 = 0 \end{cases} \tag{B.8}$$

where, ω_i and F_i denote respectively the actuator i angular velocity vector and its corresponding contact

force vector. The twelve components of the four angular velocity vectors ω_i can be described as follows,

$$\begin{bmatrix} \omega_1 \\ \omega_2 \\ \omega_3 \\ \omega_4 \end{bmatrix} = \begin{bmatrix} \omega_{1x} & \omega_{1y} & \omega_{1z} \\ \omega_{2x} & \omega_{2y} & \omega_{2z} \\ \omega_{3x} & \omega_{3y} & \omega_{3z} \\ \omega_{4x} & \omega_{4y} & \omega_{4z} \end{bmatrix} \tag{B.9}$$

It's convenient to define more equations in order to obtain the referred balanced solution. Analysing a regular tetrahedron plane normal vectors, one verifies that the dot product between any two of these normal vectors are related according to a constant $a = -\frac{1}{3}$. Therefore, taking advantage of the regular tetrahedral elegant geometry consider six more equations ensuring that the resultant four actuator rotation axis vectors are related according to the same relation, as follows,

$$\begin{cases} \omega_1.\omega_2 = a \\ \omega_1.\omega_3 = a \\ \omega_1.\omega_4 = a \\ \omega_2.\omega_3 = a \\ \omega_2.\omega_4 = a \\ \omega_3.\omega_4 = a \end{cases} \tag{B.10}$$

The combination of (B.8) and (B.10) gives a system of ten equations with respect to twelve unknowns, therefore, this is still an under-determined system and multiple solutions exist. Nevertheless using MATLAB® MuPAD software all the solutions of such a system can be easily computed. Choosing one of the obtained solutions yields,

$$\begin{bmatrix} \omega_{1x} \\ \omega_{1y} \\ \omega_{1z} \end{bmatrix} = \begin{bmatrix} 1/2 - \frac{\sqrt{3}}{6} \\ \frac{\sqrt{3}}{6} + 1/2 \\ \frac{-\sqrt{3}}{3} \end{bmatrix}, \begin{bmatrix} \omega_{2x} \\ \omega_{2y} \\ \omega_{2z} \end{bmatrix} = \begin{bmatrix} \frac{-\sqrt{3}}{6} - 1/2 \\ 1/2 - \frac{\sqrt{3}}{6} \\ \frac{\sqrt{3}}{3} \end{bmatrix}, \begin{bmatrix} \omega_{3x} \\ \omega_{3y} \\ \omega_{3z} \end{bmatrix} = \begin{bmatrix} \frac{\sqrt{3}}{6} - 1/2 \\ \frac{\sqrt{3}}{6} - 1/2 \\ \frac{-\sqrt{3}}{3} \end{bmatrix}, \begin{bmatrix} \omega_{4x} \\ \omega_{4y} \\ \omega_{4z} \end{bmatrix} = \begin{bmatrix} \frac{\sqrt{3}}{6} + 1/2 \\ \frac{\sqrt{3}}{6} - 1/2 \\ \frac{\sqrt{3}}{3} \end{bmatrix} \tag{B.11}$$

The code used for obtaining such solution is described as follows,

```
eqn1 := (2887*v1x)/5000 - (2887*v1y)/5000 - (2887*v1z)/5000=0: %Plane constraint 1
eqn2 := (2887*v2x)/5000 + (2887*v2y)/5000 + (2887*v2z)/5000=0: %Plane constraint 2
eqn3 := (2887*v3y)/5000 - (2887*v3x)/5000 - (2887*v3z)/5000=0: %Plane constraint 3
eqn4 := (2887*v4z)/5000 - (2887*v4y)/5000 - (2887*v4x)/5000=0: %Plane constraint 4
eqn5 := v1x*v2x + v1y*v2y + v1z*v2z=a: %Tetrahedral geometry vector relation 1
eqn6 := v1x*v3x + v1y*v3y + v1z*v3z=a: %Tetrahedral geometry vector relation 2
eqn7 := v1x*v4x + v1y*v4y + v1z*v4z=a: %Tetrahedral geometry vector relation 3
eqn8 := v2x*v3x + v2y*v3y + v2z*v3z=a: %Tetrahedral geometry vector relation 4
eqn9 := v2x*v4x + v2y*v4y + v2z*v4z=a: %Tetrahedral geometry vector relation 5
eqn10 :=  v3x*v4x + v3y*v4y + v3z*v4z=a: %Tetrahedral geometry vector relation 6
eqn11 := sqrt(v1x^2+v1y^2+v1z^2)=1: %Unit norm requirement vector 1
eqn12 := sqrt(v2x^2+v2y^2+v2z^2)=1: %Unit norm requirement vector 2
eqn13 := sqrt(v3x^2+v3y^2+v3z^2)=1: %Unit norm requirement vector 3
eqn14 := sqrt(v4x^2+v4y^2+v4z^2)=1: %Unit norm requirement vector 3

assume(a =-1/3): % Assume the constant relation of tetrahedral vectors geometry

solve({eqn1,eqn2,eqn3,eqn4,eqn5,eqn6,eqn7,eqn8,eqn9,eqn10,eqn11,eqn12,eqn13,eqn14},
[v1x,v1y,v1z,v2x,v2y,v2z,v3x,v3y,v3z,v4x,v4y,v4z,a],IgnoreAnalyticConstraints)
```

Figures B.4 and B.5 represent the obtained solution.

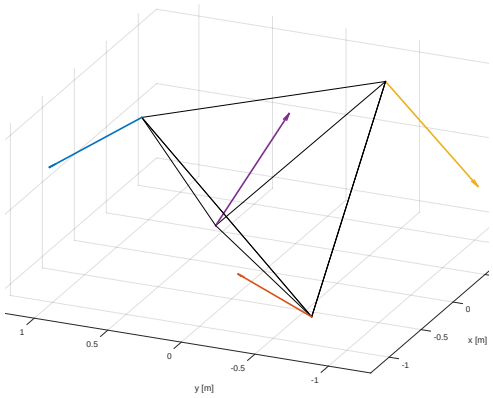

Figure B.4: Actuators rotation axes with respect to its respective contact points

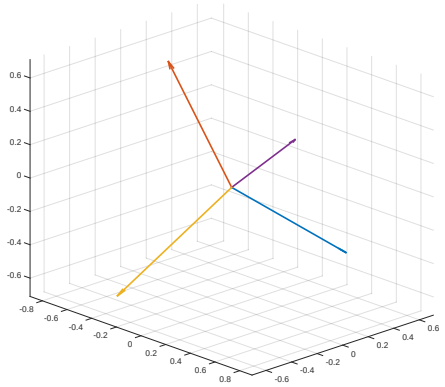

Figure B.5: Actuators rotation axes with respect to origin

Appendix C

Quaternions

This Appendix provides a brief description regarding quaternion notation. The following contents are a summary of the required concepts to develop a SACS with respect to quaternion notation, for further details see [16] and [6].

Quaternion notation makes use of Euler's theorem, stating that two reference frames are always related by an unique rotation about a single line through their common origin. This line is called the *Euler axis* and the referred unique rotation corresponding angle is denoted as *principal angle*. This important theorem allows to describe frame rotations with less variables compared to *Euler angles*.

Let $\hat{u}$ be the unit vector along Euler axis and v be an arbitrary vector in space. Hence v can be decomposed in two components, one $v_\perp$ normal to $\hat{u}$ and another $v_\parallel$ parallel to $\hat{u}$, so that the following relation is valid,

$$v = v_\parallel + v_\perp \tag{C.1}$$

Therefore, the v component along $\hat{u}$ can be computed from the dot product as follows,

$$v_\parallel = (v \cdot \hat{u})\hat{u} \tag{C.2}$$

Combining (C.1) and (C.2) yields,

$$v_\perp = v - (v \cdot \hat{u})\hat{u} \tag{C.3}$$

Consider that v' is obtained by rotating v through an angle θ around $\hat{u}$, as it can be seen in Figure C.1

The rotation of v keeps the magnitude of $v_\perp$ and its components along the direction $\hat{u}$ unchanged, see (C.4) and (C.5).

$$||v'_\perp|| = ||v_\perp|| \tag{C.4}$$

$$||v'_\parallel|| = (v \cdot \hat{u}).\hat{u} \tag{C.5}$$

Which means that having rotated $v'_\perp$ about $\hat{u}$, results in two components, namely, $||v'_\perp||cos(\theta)$ along $v_\perp$ and $||v'_\perp||sin(\theta)$ along the normal vector perpendicular to $\hat{u}v$ plane. Let $\hat{u}v$ be the plane defined by $\hat{u}$ and

v vectors. Moreover let $\hat{w}$ be the unit vector normal to $\hat{u}v$ plane.

$$\hat{w} = \hat{u} \times \frac{v_\perp}{||v_\perp} \tag{C.6}$$

Consider (C.7) illustration in Figure C.1.

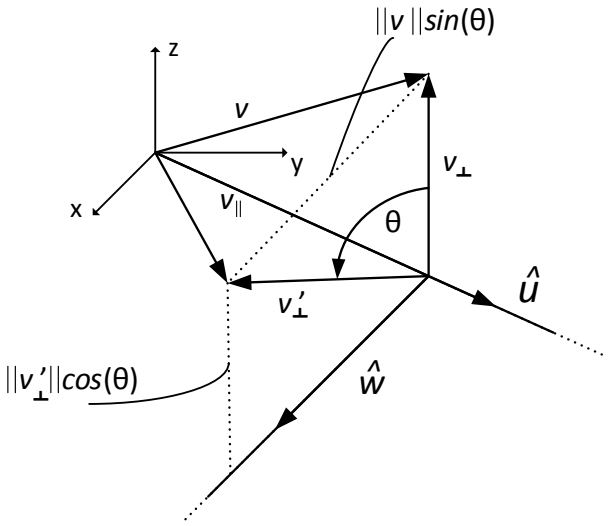

Figure C.1: Vector rotation with respect to Euler axis

$$v'_\perp = ||v'_\perp||cos(\theta)\frac{v_\perp}{||v_\perp||} + ||v'_\perp||sin(\theta)\frac{\hat{u} \times v_\perp}{||v_\perp||} \tag{C.7}$$

Making use of the relation (C.4), (C.7) yields,

$$v'_\perp = cos(\theta).v_\perp + sin(\theta).\hat{u} \times v_\perp \tag{C.8}$$

Having that,

$$\hat{u} \times v_\perp = \hat{u} \times [v - v_\parallel] = \hat{u} \times v \tag{C.9}$$

and since $v_\parallel$ is parallel to $\hat{u}$, combining this with (C.3) yields,

$$v'_\perp = cos(\theta)[v - (v.\hat{u}\hat{u})] + sin(\theta)(\hat{u} \times v) \tag{C.10}$$

Finally having in mind that $v' = v'_\perp + v'_\parallel$, one finds, by making use of (C.5) and (C.10) that,

$$v' = cos(\theta)v + (1 - cos(\theta))(\hat{u}.v) + sin(\theta)(\hat{u} \times v) \tag{C.11}$$

Expression (C.11) allows to express a vector v rotation about a line with respect to an unique rotation θ. Hence, it is possible to write a body fixed Cartesian frame $x'y'z'$ from the inertial xyz frame by a

single rotation through the principal angle θ about the *Euler axis* $\hat{u}$. The unit vectors $\vec{e_x}$,$\vec{e_y}$,$\vec{e_z}$ are thereby rotated into $\vec{e'}_x$,$\vec{e'}_y$ and $\vec{e'}_z$. Moreover these two sets of unit vectors are related as,

$$\begin{aligned}
\vec{e'}_x &= cos(\theta)\ \vec{e_x} + (1 - cos(\theta))(\hat{u}\ .\ \vec{e_x})\ \hat{u} + sin(\theta)(\hat{u} \times \vec{e_x}) \\
\vec{e'}_y &= cos(\theta)\ \vec{e_y} + (1 - cos(\theta))(\hat{u}\ .\ \vec{e_y})\ \hat{u} + sin(\theta)(\hat{u} \times \vec{e_y}) \\
\vec{e'}_z &= cos(\theta)\ \vec{e_z} + (1 - cos(\theta))(\hat{u}\ .\ \vec{e_z})\ \hat{u} + sin(\theta)(\hat{u} \times \vec{e_z})
\end{aligned} \tag{C.12}$$

Writing *Euler axis* unit vector $\hat{u}$ with respect to the terms of its direction cosines, namely, l,m and n along the original xyz axes yields,

$$\hat{u} = l\ \vec{e_x} + m\ \vec{e_y} + n\ \vec{e_z} \tag{C.13}$$

Substituting (C.13) into (C.12) yields,

$$\begin{aligned}
\vec{e'}_x &= [l^2(1 - cos\ \theta) + lcos\ \theta]\ \vec{e_x} + [lm(1 - cos\ \theta) + nsin\ \theta]\ \vec{e_y} + [ln(1 - cos\ \theta) + msin\ \theta]\ \vec{e_z} \\
\vec{e'}_y &= [lm(1 - cos\ \theta) - nsin\ \theta]\ \vec{e_x} + [m^2(1 - cos\ \theta) + cos\ \theta]\ \vec{e_y} + [mn(1 - cos\ \theta) + lsin\ \theta]\ \vec{e_z} \\
\vec{e'}_z &= [ln(1 - cos\ \theta) + msin\ \theta]\ \vec{e_x} + [mn(1 - cos\ \theta) + lsin\ \theta]\ \vec{e_y} + [n^2(1 - cos\ \theta) + cos\ \theta]\ \vec{e_z}
\end{aligned} \tag{C.14}$$

Therefore, considering (C.14), it's seen that a rotation matrix between frames xyz and $x'y'z'$ can be defined with respect to the *Euler axis* $\hat{u}$ and the principal angle θ. Thus the referred rotation matrix is given by (C.15).

$$[Q]_{xyz\ to\ x'y'z'} = \begin{bmatrix}
l^2(1 - cos\ \theta) + lcos\ \theta & lm(1 - cos\ \theta) + nsin\ \theta & ln(1 - cos\ \theta) + msin\ \theta \\
lm(1 - cos\ \theta) - nsin\ \theta & m^2(1 - cos\ \theta) + cos\ \theta & mn(1 - cos\ \theta) + lsin\ \theta \\
ln(1 - cos\ \theta) + msin\ \theta & mn(1 - cos\ \theta) + lsin\ \theta & n^2(1 - cos\ \theta) + cos\ \theta
\end{bmatrix} \tag{C.15}$$

Hence it is possible to describe any rotation between frames with respect to four parameters, namely, three components of the *Euler axis* and the principal angle θ.

Quaternion notation were introduced by Hamilton[1] describing a body frame orientation in a simple yet elegant form.

As the name implies, quaternions are composed of four components,

$$\hat{q} = \begin{Bmatrix} q_1 \\ q_2 \\ q_3 \\ q_4 \end{Bmatrix} = \begin{Bmatrix} g \\ q_4 \end{Bmatrix} \tag{C.16}$$

where g is known as the vector part and q_4 is known as the scalar part.

A quaternion norm $||\hat{q}||$ is defined as

$$||\hat{q}|| = \sqrt{q_1^2 + q_2^2 + q_3^2 + q_4^2} \tag{C.17}$$

[1] On October 16, 1843, when Hamilton was on his way to the Royal Irish Academy where he was going to preside at a council meeting. As he walked along the Royal Canal with his wife, the concepts behind quaternions were taking shape in his mind. When the answer dawned on him, Hamilton could not resist the urge to carve the formula for the quaternions, $i^2 = j^2 = k^2 = ijk = -1$, which are the basis of quaternion notation

This study considers only *unit quaternions*. Hence, quaternions are defined as,

$$q = sin\frac{\theta}{2} \,.\, \hat{u} \quad , \quad q_4 = cos\frac{\theta}{2} \tag{C.18}$$

expanding with respect to the $\hat{u}$ components yields,

$$q_1 = l\ sin\frac{\theta}{2} \quad , \quad q_2 = m\ sin\frac{\theta}{2} \quad , \quad q_3 = n\ sin\frac{\theta}{2} \quad , \quad q_4 = cos\frac{\theta}{2} \tag{C.19}$$

C.1 Quaternion relation with rotation matrices

According to (C.19) it is possible to write matrix (C.15) with respect to the quaternion components. Hence (C.15) can be written as follows,

$$[Q]_{xyz\ to\ x'y'z'} = \begin{bmatrix} q_1^2 - q_2^2 - q_3^2 + q_4^2 & 2(q_1.q_2 + q_3.q_4) & 2(q_1.q_3 - q_2.q_4) \\ 2(q_1.q_2 - q_3.q_4) & -q_1^2 + q_2^2 - q_3^2 + q_4^2 & 2(q_2.q_3 + q_1.q_4) \\ 2(q_1.q_3 + q_2.q_4) & 2(q_2.q_3 - q_1.q_4) & -q_1^2 - q_2^2 + q_3^2 + q_4^2 \end{bmatrix} \tag{C.20}$$

(C.20) verifies the required orthogonality property of a rotation matrix, see (C.21).

$$[Q]_{xyz\ to\ x'y'z'} \,.\, [Q]^T_{xyz\ to\ x'y'z'} = 1 \tag{C.21}$$

The unit quaternion can also be obtained from the direction cosine matrix $[Q]_{xyz\ to\ x'y'z'}$. This procedure is described as follows.

First obtain the following matrix,

$$[k] = \frac{1}{3}\begin{bmatrix} Q_{11} - Q_{22} - Q_{33} & Q_{21} + Q_{12} & Q_{31} + Q_{13} & Q_{23} - Q_{32} \\ Q_{21} + Q_{12} & -Q_{11} + Q_{22} - Q_{33} & Q_{32} + Q_{23} & Q_{31} - Q_{13} \\ Q_{31} + Q_{13} & Q_{32} + Q_{23} & -Q_{11} - Q_{22} + Q_{33} & Q_{12} - Q_{21} \\ Q_{23} + Q_{32} & Q_{31} - Q_{13} & Q_{12} - Q_{21} & Q_{11} + Q_{22} + Q_{33} \end{bmatrix} \tag{C.22}$$

Then, compute the eigenvalues of the obtained matrix. The eigenvector corresponding to the largest eigenvalue corresponds to the unit quaternion $\hat{q}$.

C.2 Quaternion multiplication

Analogously to rotation matrices multiplication, it is useful to compute in quaternion notation the resultant rotation obtained from combining two consecutive rotations. Therefore, such two rotations can be expressed in quaternion terminology as $[A(q)]$ and $[A(q')]$. Hence, the following expression gives the overall attitude rotation computation in terms of quaternion terminology,

$$[A(q'')] = [A(q')][A(q)] \tag{C.23}$$

Using quaternion properties, one can extract q'' value from $[A(q'')]$, hence,

$$q'' = qq' = \begin{bmatrix} q_1'' \\ q_2'' \\ q_3'' \\ q_4'' \end{bmatrix} = \begin{bmatrix} (q_1 q_4' + q_2 q_3' - q_3 q_2' + q_4 q_1')\hat{i} \\ (-q_1 q_3' + q_2 q_4' + q_3 q_1' + q_4 q_2')\hat{j} \\ (q_1 q_2' - q_2 q_1' + q_3 q_4' + q_4 q_3')\hat{k} \\ (-q_1 q_1' - q_2 q_2' - q_3 q_3' + q_4 q_4') \end{bmatrix} \tag{C.24}$$

which can be written in a matrix multiplication form as (C.25), see [10] for further details.

$$\begin{bmatrix} q_1'' \\ q_2'' \\ q_3'' \\ q_4'' \end{bmatrix} = \begin{bmatrix} q_4' & q_3' & -q_2' & q_1' \\ -q_3' & q_4' & q_1' & q_2' \\ q_2' & -q_1' & q_4' & q_3' \\ -q_1' & -q_2' & -q_3' & q_4' \end{bmatrix} \begin{bmatrix} q_1 \\ q_2 \\ q_3 \\ q_4 \end{bmatrix} \tag{C.25}$$

C.3 Quaternion Time derivative

The quaternion time derivative is an useful tool when working with quaternions to describe a body angular velocity and angular acceleration according to quaternion notation.

$$\frac{d}{dt}\hat{q} = \frac{1}{2}[\Omega]\hat{q} \tag{C.26}$$

The quaternion time derivative is illustrated in (C.26), being Ω matrix described in (C.27), where ω_x,ω_y and ω_z are the body frame angular velocity components

$$[\Omega(\omega)] = \begin{bmatrix} 0 & \omega_z & -\omega_y & \omega_x \\ -\omega_z & 0 & \omega_x & \omega_y \\ \omega_y & -\omega_x & 0 & \omega_z \\ -\omega_x & -\omega_y & -\omega_z & 0 \end{bmatrix} \tag{C.27}$$

Appendix D

Redundant RWs arrangement optimal criteria

This Appendix describes the torque combination for redundant RW arrangements using Moore-Penrose pseudoinverse.

It is known that, two distinct values of τ_{rw} may produce the same τ_{ctrl}, hence their difference, $\Delta\tau_{rw}$, must satisfy (D.1).

$$\mathsf{W}_{rw}\Delta\tau_{rw} = 0 \tag{D.1}$$

Consequently $\Delta\tau_{rw}$ must lie in the W_{rw} null space, which is $(n-3)$ dimensional, assuming W_{rw} is full rank.

The Moore-Penrose pseudoinverse method enables torque commands distribution computation for redundant RW arrangements. Let W_{rw} pseudoinverse be denoted as $\mathsf{W}_{rw}^{\dagger}$.

Moreover considering W_{rw} to be full rank, the Moore-Penrose pseudoinverse is given by,

$$\mathsf{W}_{rw}^{\dagger} = \mathsf{W}_{rw}^{T}(\mathsf{W}_{rw}\mathsf{W}_{rw}^{T})^{-1} \tag{D.2}$$

Hence, it is possible to write,

$$\tau_{rw} = \mathsf{W}_{rw}^{\dagger}\tau_{ctrl} \tag{D.3}$$

The most general solution for RWs torque coefficients satisfying (3.29) is given by (D.4).

$$\tau_{rw} = \mathsf{W}_{rw}^{\dagger}\tau_{ctrl} + n_n = \mathsf{W}_{rw}^{T}(\mathsf{W}_{rw}\mathsf{W}_{rw}^{T})^{-1}\tau_{ctrl} + n_n \tag{D.4}$$

where n_n denotes an arbitrary vector in the null space of W_{rw}. Computing the RWs torques Euclidean norm yields,

$$||\tau_{rw}||^2 = ||\mathsf{W}_{rw}^{T}(\mathsf{W}_{rw}\mathsf{W}_{rw}^{T})^{-1}\tau_{ctrl}||^2 + 2(\tau_{ctrl})^{T}(\mathsf{W}_{rw}\mathsf{W}_{rw}^{T})^{-1}\mathsf{W}_{rw}\ n_n + ||n_n||^2 \tag{D.5}$$

Therefore according to the the null space definition, (D.5) yields,

$$||\tau_{rw}||^2 = ||\mathsf{W}_{rw}^T(\mathsf{W}_{rw}\mathsf{W}_{rw}^T)^{-1}\tau_{ctrl}||^2 + ||n_n||^2 \tag{D.6}$$

Analysing (D.6) one concludes that the Euclidean norm L_2 is minimized when $n_n = 0$, i.e., the Moore-Penrose pseudoinverse verifies the Euclidean norm requirement for distributing the RWs torques. For a complete proof of the result and appliances in RWs satellite torque optimization, see respectively [2] and [22].

Appendix E

Generic DC motor model

This Appendix addresses the dynamic model derivation of a DC motor. This model is a reduced order approximation of a DC motor complete model, nevertheless it describes its essential behaviour.

The following model was obtained according to distinct approaches for a DC motor model, e.g. [25] and [30]. Figure E.1 shows a generic electric scheme of a DC motor with respect to its electrical parameters. Considering Figure E.1, the motor circuit equation can be found based on *KVL*. Writing the

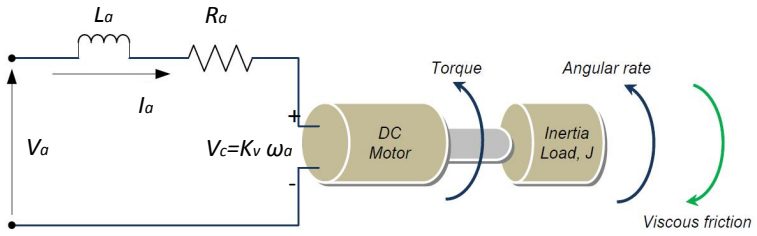

Figure E.1: Electrical motor equivalent scheme

armature electrical differential equations yields,

$$V_a = (R_a + \frac{d}{dt}L_a)I_a + V_c \tag{E.1}$$

where, V_a and I_a denote respectively the armature voltage and the armature current and R_a and L_a denote respectively the armature resistance and the armature inductance. Voltage V_c denotes the back electromotive force which is proportional to the angular velocity ω_a, as shown in (E.2).

$$V_c = k_v \omega_a \tag{E.2}$$

where, k_v refers to the motor velocity constant, varying according to motor physical construction. The motor mechanical torque balance is described by,

$$\begin{aligned} \tau_m &= (\tfrac{d}{dt}J_m + F_m)\omega_a + \tau_L \\ \tau_m &= k_t I_a \end{aligned} \tag{E.3}$$

where τ_m and τ_L denote respectively the driving torque and load reaction torque, whereas J_m, F_m and k_t are respectively the motor shaft moment of inertia, the motor viscous friction coefficient and the torque constant. Combining (E.1), (E.2) and (E.3) yields,

$$\begin{aligned} \tfrac{d}{dt} I_a &= -\tfrac{R_a}{L_a} I_a - \tfrac{k_v}{L_a}\omega_a + \tfrac{V_a}{L_a} \\ \tfrac{d}{dt}\omega_a &= \tfrac{k_t}{J_m} I_a - \tfrac{F_m}{J_m}\omega_a - \tfrac{\tau_L}{J_m} \end{aligned} \tag{E.4}$$

Analysing (E.4) it is straightforward to obtain a DC motor generic state-space model matrices, as follows,

$$\frac{d}{dt}\begin{bmatrix} I_a \\ \omega_a \end{bmatrix} = \underbrace{\begin{bmatrix} -\frac{R_a}{L_a} & \frac{k_v}{L_a} \\ \frac{k_t}{J_m} & -\frac{F_m}{J_m} \end{bmatrix}}_{A} \begin{bmatrix} I_a \\ \omega_a \end{bmatrix} + \underbrace{\begin{bmatrix} \frac{1}{L_a} & 0 \\ 0 & -\frac{1}{J_m} \end{bmatrix}}_{B} \begin{bmatrix} V_a \\ \tau_L \end{bmatrix} \tag{E.5}$$

$$\begin{bmatrix} y_1 \\ y_2 \end{bmatrix} = \underbrace{\begin{bmatrix} 1 & 0 \\ 0 & 1 \end{bmatrix}}_{C} \begin{bmatrix} I_a \\ \omega_a \end{bmatrix} + \underbrace{\begin{bmatrix} 0 & 0 \\ 0 & 0 \end{bmatrix}}_{D} \tag{E.6}$$

Equations (E.5) and (E.6) denote the state space equations which can be expressed symbolically as,

$$\begin{aligned} \dot{x} &= Ax + Bu \\ y &= Cx + Du \end{aligned} \tag{E.7}$$

Computing (E.4) Laplace transform expression yields,

$$sI_a(s) = -\frac{R_a}{L_a} I_a(s) - \frac{k_v}{L_a}\Omega_a(s) + \frac{1}{L_a} V_a(s) \tag{E.8}$$

$$s\Omega_a(s) = \frac{k_t}{J_m} I_a(s) - \frac{F_m}{J_m}\Omega_a(s) - \frac{1}{J_m}\tau_L(s) \tag{E.9}$$

Regarding (E.8) and (E.9) a system block diagram can be obtained, see Figure E.2.

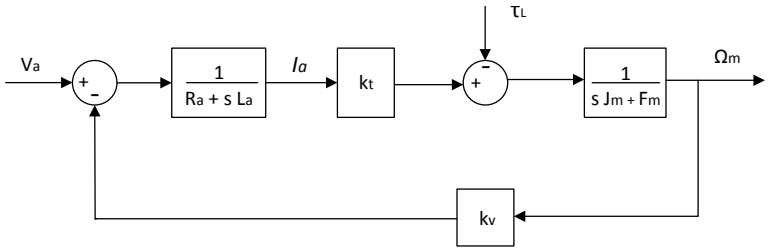

Figure E.2: Motor dynamics block diagram

Motors usually have gear ratios between the load velocity and motor shaft velocity in order to improve their efficiency. If such ratio didn't exist, the inclusion of the load inertia would be straightforward and required only the load moment of inertia sum to the motor moment of inertia ($J_{eq} = J_m + J_L$). Nevertheless, if such a gear ratio exist, the equivalent load moment of inertia seen at the motor frame is described as,

$$J_{eq} = (J_m + \frac{J_L}{k_r^2}) \tag{E.10}$$

where, k_r denotes the gear ration given by,

$$k_r = \frac{\omega_m}{\omega_L} \tag{E.11}$$

If the load inertia frame doesn't match the motor frame, it is required to perform an inertia tensor transformation, see (E.12).

$$J_L^M = R_L^M J_L (R_L^M)^T \tag{E.12}$$

Let R_L^M denote the rotation matrix from the load frame to the motor frame.

An example of a DC motor state-space model embedded in an angular velocity control loop is depicted in Figure E.3. The "Voltage limit saturation" and "Slew-rate limitation" blocks intend to model the motor power supply physical limits.

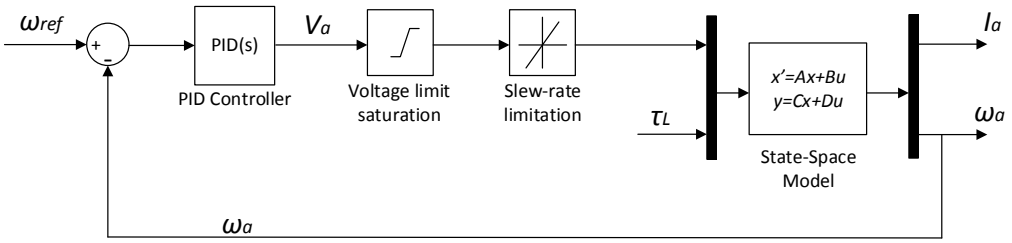

Figure E.3: DC motor state-space model with PID controller and PS limitations